

# Magnetic Nanocomposites Containing Low and Medium-Molecular Weight Chitosan for Dye Adsorption: Hydrophilic Property Versus Functional Groups

Masouma Mirzai

Bu-Ali Sina University: Bu Ali Sina University

Simin Asadabadi (✉ [s.asadabadi@basu.ac.ir](mailto:s.asadabadi@basu.ac.ir))

Bu-Ali Sina University: Bu Ali Sina University <https://orcid.org/0000-0001-8992-6894>

---

## Research Article

**Keywords:** Chitosan molecular weight, Magnetic nanocomposites, DTPA, Graphene oxide, Basic blue 41, Central Composite Design

**Posted Date:** July 8th, 2021

**DOI:** <https://doi.org/10.21203/rs.3.rs-684636/v1>

**License:** © ⓘ This work is licensed under a Creative Commons Attribution 4.0 International License.

[Read Full License](#)

---

**Version of Record:** A version of this preprint was published at Journal of Polymers and the Environment on October 4th, 2021. See the published version at <https://doi.org/10.1007/s10924-021-02300-5>.

# Magnetic Nanocomposites Containing Low and Medium-Molecular Weight Chitosan for Dye Adsorption: Hydrophilic property versus functional groups

Masouma Mirzai, Simin Asadabadi\*

*Department of Applied Chemistry, Faculty of Chemistry, Bu–Ali Sina University, Hamedan 6517838695, Iran*

Tel: +98 81 38282807

Fax: +98 81 38380709

\*Corresponding author: (Dr. Simin Asadabadi), E-mail address: [s.asadabadi@basu.ac.ir](mailto:s.asadabadi@basu.ac.ir)

Corresponding author's ORCID ID: 0000-0001-8992-6894

## ABSTRACT

The azo dye removal from polluted water is vital from a sustainable viewpoint. In this study, we investigated the influence of chitosan molecular weight on the adsorptive removal of basic blue 41. For preparing nanocomposite containing medium-molecular weight chitosan (NC(M)), cross-linking of chitosan was done using diethylenetriaminepentaacetic acid, silica-modified magnetite nanoparticles and graphene oxide. Techniques including FT-IR, XRD, FESEM, TGA/DTG, VSM and N<sub>2</sub> adsorption/desorption isotherm were applied for characterization of NC(M). The adsorption behavior of synthesized NC(M) was compared with as-prepared adsorbent containing low-molecular weight chitosan (NC(L)) (Asadabadi 2021). The experimental design was carried out using the Central Composite Design. The effect of initial pH, temperature and adsorbent concentration on the percentage of dye removal were examined and the optimum values of variables were determined. Despite NC(M) which had maximum 31% dye removal, NC(L) led to approximately 95% adsorptive removal at optimum conditions. An increase in the monomer number of chitosan caused to reduce hydrophilic property of NC(M), which in turn resulted in a repulsion force between adsorbent and dye. However, H-bonding, coulumbic attraction and pi-stacking interactions contributed in the adsorption mechanism of NC(L). The kinetics study showed that about 30 min necessitated reaching the equilibrium and the rate-limiting steps changed from film diffusion to intra-particle diffusion as time passed. The kinetics data were satisfactorily fitted by the modified pseudo-n-order model. The maximum adsorption capacity of NC(L) was obtained 55.87 mg·g<sup>-1</sup>. The modified Langmuir-Freundlich isotherm was the best model to reproduce data. NC(L) was recovered seven times without dramatic changes in its adsorption efficiency.

**Keywords** *Chitosan molecular weight; Magnetic nanocomposites; DTPA; Graphene oxide; Basic blue 41, Central Composite Design*

## Introduction

Remarkable increase of the demand for treated water is resulted from the fast growth of population and industrial development [1, 2]. Discharging effluents of dyes from textile, leather,

paper and cosmetics industries is one of the most concerning issues [3, 4]. Most synthetic dyes are non-biodegradable producing colored water, absorb/reflect sunlight and produce carcinogenic bio-transformed intermediates thus they imperil the aquatic and human life [5]. Azo, indigoid and anthraquinoid are the major class of dyes. Among them, azo dye molecules have a conjugated system of aromatic rings and nitrogen double bonds with strong  $\pi \rightarrow \pi^*$  transitions in the UV-Vis region [5]. Aromatic amines can be formed because of azo bond cleavage and reduction creating severe environmental problems. Different techniques such as reverse osmosis, chemical oxidation, adsorption, coagulation, electrochemical methods and their combinations can be used for treatment of the industrial azo dyes [6–8]. Cost, efficiency, ease of operation, the amount of secondary waste and facile recovery make adsorption process as a suitable approach for effluent treatment [9]. Developing a cost-effective, biodegradable and efficient adsorbent has been a big challenge for researchers to remove dangerous azo dyes [10, 11]. Graphene-based materials, hydrogels and bio-polymers can be utilized for dye adsorption [12, 13].

Chitosan (CS) is a natural polysaccharide (Poly- $\beta$ -(1 $\rightarrow$ 4)-D-glucosamine with randomly distributed N-acetyl-D-glucosamine units) can be obtained from chitin and has been considered for tackling the problem of contaminated water [14, 15]. Although this bio-polymer has abundant functional groups, its application is limited by low adsorption capacity, inadequate hydrophilicity and poor recyclability [16]. Grafting and chemical cross-linking of chitosan is considered as a route to overcome the disadvantages of raw chitosan [17–19]. For instance, using aminopolycarboxylic acid such as nitrilotriacetic acid (NTA), ethylenediaminetetraacetic acid (EDTA) and diethylenetriaminepentaacetic acid (DTPA) can improve adsorption properties of chitosan [20–22]. However, the synergism effect is restricted since there is only a single adsorption mechanism, mainly electrostatic attraction. Thus, adding a compound possessing aromatic rings to the chitosan cause to have the  $\pi$ - $\pi$  stacking and cation- $\pi$  interaction between cationic azo dye and sorbent [23]. Graphene oxide (GO) with aromatic rings are a good candidate for this purpose. GO nanosheets have functional groups of carboxyl, hydroxyl and epoxy which give GO outstanding surface characteristics and attract researchers' attention for improving the properties of chitosan [18, 24]. For example, Jiang et al. [18] synthesized a nanocomposite consisting thiol-modified chitosan and magnetic graphene oxide and used it for effective adsorption of methyl blue and crystal violet dyes. Adsorbent was successfully recycled five times.

Technology of magnetic separation is one of the reasonable approach to efficient recovery

of chitosan. One of the best materials used for magnetization is magnetite nanoparticles ( $\text{Fe}_3\text{O}_4$ ) because of its superparamagnetic property, biocompatibility and low toxicity [25]. In many cases, surface modification of  $\text{Fe}_3\text{O}_4$  is important for two reasons; (I) protection of magnetite from oxidation and (II) generating surface functional groups for attaching to precursors of adsorbent [26]. In 2021, Liu et al. [27] synthesized a magnetic amphiphilic chitosan-based adsorbent having benzyl groups and applied it for removing azo dyes. The presence of benzyl groups and magnetic chitosan resulted in a high adsorption because of synergism effect.

Another factor having influence on the adsorption efficiency is the molecular weight of chitosan. Commercial chitosan can be supplied in low (50-190 kDa), medium (190–310 kDa) and high-molecular weight (310-375 kDa). On the one hand, an increase in the monomer unit leads to the increase in the functional groups. On the other hand, hydrophilic property changes by molecular weight [7, 27, 28]. To show importance of functional groups and hydrophilicity, a magnetic medium-molecular weight chitosan adsorbent was prepared and used for adsorption of basic blue 41 (as an azo dye pollutant). A comparison was made with as-prepared adsorbent containing low-molecular weight chitosan [20]. Graphene oxide and DTPA were used for cross-linking of chitosan and magnetization was done by silica-modified magnetite nanoparticles. Central Composite Design based on the Response Surface Methodology was applied for design of experiments and optimization. Kinetics and equilibrium studies were performed at optimum conditions and the rate limiting steps were determined. Different kinetics and isotherm models were used for fitting the experimental data. Cyclic recovery of nanocomposite was tested in different medium in the presence of ultrasonic waves.

## Materials and Methods

### Materials

Basic blue 41 (BB41, known as cationic blue 41) was supplied from Alvan Sabet Company with 98% purity and was used as the contaminant. Basic blue 41 is an azo dye with the chemical formula of  $\text{C}_{20}\text{H}_{26}\text{N}_4\text{O}_6\text{S}_2$  (the color index of 11105). This dye allows strong transition of  $\pi \rightarrow \pi^*$  in the UV-Vis region with maximum absorption at 508 nm. The chemical structure and UV-Vis absorption spectrum of BB41 is presented in Fig. 1.

**Fig. 1** Structure and UV-Vis absorption spectrum of basic blue 41 at concentration of  $10.0 \text{ mg}\cdot\text{L}^{-1}$  and pH of 6.5

Solutions were prepared with deionized water having electrical conductivity of  $0.08 \mu\text{S}\cdot\text{cm}^{-1}$ . Chemicals were purchased from Sigma-Aldrich and Merck companies and used without

further purification. Specifications of chemicals are summarized in Table 1.

**Table 1** Specifications of used chemicals

Chemicals	Chemical Formula	Molecular weight (g·mol <sup>-1</sup> )	Purity (%)	Application
Iron(III) chloride hexahydrate	FeCl <sub>3</sub> ·6H <sub>2</sub> O	271.33	99	Synthesis of Fe <sub>3</sub> O <sub>4</sub>
Sodium sulfite	Na <sub>2</sub> SO <sub>3</sub>	126.04	95.5	Synthesis of Fe <sub>3</sub> O <sub>4</sub>
Fuming hydrochloric acid	HCl	36.46	37	Synthesis of Fe <sub>3</sub> O <sub>4</sub> , adjusting pH
Ammonium hydroxide	NH <sub>4</sub> OH	35.04	28	Synthesis of Fe <sub>3</sub> O <sub>4</sub>
Absolute ethanol	EtOH	46.07	100	Modification of Fe <sub>3</sub> O <sub>4</sub>
Tetraethyl orthosilicate (TEOS)	SiC <sub>8</sub> H <sub>24</sub> O <sub>4</sub>	208.33	99	Modification of Fe <sub>3</sub> O <sub>4</sub>
Sodium hydroxide	NaOH	40.00	99	Modification of Fe <sub>3</sub> O <sub>4</sub> , adjusting pH
3-aminopropyltriethoxysilane (APTES)	H <sub>2</sub> N(CH <sub>2</sub> ) <sub>3</sub> Si(OC <sub>2</sub> H <sub>5</sub> ) <sub>3</sub>	221.37	98	Modification of Fe <sub>3</sub> O <sub>4</sub> @SiO <sub>2</sub>
Toluene	C <sub>7</sub> H <sub>8</sub>	92.14	99.9	Modification of Fe <sub>3</sub> O <sub>4</sub> @SiO <sub>2</sub>
Low-molecular weight chitosan (CS(L))	(C <sub>6</sub> H <sub>11</sub> NO <sub>4</sub> ) <sub>n</sub>	50 to 190 kDa	75-85% deacetylated	Synthesis of nanocomposite
Medium-molecular weight chitosan (CS(M))	(C <sub>6</sub> H <sub>11</sub> NO <sub>4</sub> ) <sub>n</sub>	190 to 310 kDa	75-85% deacetylated	Synthesis of nanocomposite
Diethylenetriaminepentaacetic acid (DTPA)	C <sub>14</sub> H <sub>23</sub> N <sub>3</sub> O <sub>10</sub>	393.35	99	Synthesis of nanocomposite
Sulfuric acid	H <sub>2</sub> SO <sub>4</sub>	98.08	98	Synthesis of graphene oxide
Orthophosphoric acid	H <sub>3</sub> PO <sub>4</sub>	98.00	85	Synthesis of graphene oxide
Graphite powder	C	-	-	Synthesis of graphene oxide
Potassium permanganate	KMnO <sub>4</sub>	158.03	99	Synthesis of graphene oxide
Hydrogen peroxide	H <sub>2</sub> O <sub>2</sub>	34.01	30	Synthesis of graphene oxide
n-hexane	C <sub>6</sub> H <sub>14</sub>	86.18	96	Solvent
N-hydroxysuccinimide (NHS)	C <sub>4</sub> H <sub>5</sub> NO <sub>3</sub>	115.09	99	Activation of carboxyl group
N,N'-dicyclohexylcarbodiimide (DCC)	C <sub>13</sub> H <sub>22</sub> N <sub>2</sub>	206.33	99	Activation of carboxyl group
N,N-dimethylformamide (DMF)	C <sub>3</sub> H <sub>7</sub> NO	73.09	99.8	Solvent
Acetic acid	CH <sub>3</sub> COOH	60.05	99.8	Solvent
Sodium dihydrogen phosphate monohydrate	NaH <sub>2</sub> PO <sub>4</sub> ·H <sub>2</sub> O,	137.99	98	Buffer preparation

## Preparation of Nanocomposites

Silica-modified magnetite, low or medium-molecular weight chitosan (CS(L) and CS(M), respectively), graphene oxide (GO) and diethylenetriaminepentaacetic acid (DTPA) were the

components of nanocomposites.

The procedures for synthesis of  $\text{Fe}_3\text{O}_4$ ,  $\text{Fe}_3\text{O}_4@\text{SiO}_2$ , modified core-shell ( $\text{Fe}_3\text{O}_4@\text{SiO}_2@\text{APTES}$ ), GO and DTPA-CS(L) and the nanocomposite with low-molecular weight chitosan (denoted as NC(L)) were described in detail in our previous study [20]. Briefly, magnetite nanoparticles ( $\text{Fe}_3\text{O}_4$ ) were prepared using acidic solution of  $\text{FeCl}_3$  (18.8 mL,  $2.0 \text{ mol}\cdot\text{L}^{-1}$ ),  $\text{Na}_2\text{SO}_3$  solution (12.5 mL,  $1.0 \text{ mol}\cdot\text{L}^{-1}$ ) and deionized water (18.8 mL). The mixture was quickly poured into  $\text{NH}_4\text{OH}$  solution (500.0 mL,  $0.85 \text{ mol}\cdot\text{L}^{-1}$ ) and stirred.  $\text{Fe}_3\text{O}_4$  nanoparticles were obtained after 30 min, washed out with deionized water and ethanol and dried at  $25.0^\circ\text{C}$  overnight [29]. Stöber method was used for modification of magnetite [30]. After mixing of absolute ethanol (160.0 mL), deionized water (40.0 mL) and  $\text{Fe}_3\text{O}_4$  (2.0000 g) in ultrasonic bath, concentrated  $\text{NH}_4\text{OH}$  solution (5.0 mL,  $14.82 \text{ mol}\cdot\text{L}^{-1}$ ) was promptly was added. TEOS (5.0 mL) was poured into the mixture very slowly and stirred at room temperature for 24 h. The particles of  $\text{Fe}_3\text{O}_4@\text{SiO}_2$  were rinsed with deionized water and ethanol and dried at room temperature for 12 h. The modified core (1.0000 g) was added into toluene (60.0 mL) and APTES (1.0 mL) was slowly poured into the vessel of reaction placed in the ultrasonic bath for 2 h. The mixture was refluxed for 24 h under temperature of  $110.0^\circ\text{C}$ . The product ( $\text{Fe}_3\text{O}_4@\text{SiO}_2@\text{APTES}$ ) was washed out by n-hexane and ethanol, successively, and dried at room temperature [31]. For preparing GO, a cooled mixture of graphite (0.5000 g),  $\text{H}_2\text{SO}_4$  and  $\text{H}_3\text{PO}_4$  (8:2 volume ratio) was treated with  $\text{KMnO}_4$  (3.0000 g). After mixing, the reagents were transferred to the oil bath ( $65.0^\circ\text{C}$ ) for 12 h. After cooling the mixture, deionized water (220.0 mL) and  $\text{H}_2\text{O}_2$  (3.0 mL of 30% w/w) were added and sonicated for 30 min. GO nanosheets were washed out by HCl (100.0 mL, 30% w/w), deionized water (100.0 mL) and ethanol, sequentially. N-hexane was used for coagulating GO sheets. The product was dried at  $40.0^\circ\text{C}$  [32]. Low or medium-molecular weight chitosan was modified by DTPA. In this regard, 0.7000 g CS(L or M) were dissolved in acetic acid (75.0 mL, 2.0 % v/v). Also, 3.6600 g DTPA and 0.4000 g N-hydroxysuccinimide (NHS) were dissolved in  $\text{NH}_4\text{OH}$  (2.0 mL, 28% w/w). Two solutions were slowly poured into the mixture of N,N-dimethylformamide (DMF, 50.0 ml) and N,N'-dicyclohexylcarbodiimide (DCC, 2.6200 g) placed in ice bath. Low temperature was crucial to prevent carboxylate anion formation. After mixing, temperature of mixture was set at  $60.0^\circ\text{C}$  and it was stirred for 12 h. DTPA-CS(L) and DTPT-(M) were washed out with deionized water and dried at  $45.0^\circ\text{C}$  for 12 h.

Nanocomposites having low and medium-molecular weight chitosan (NC(L) and NC(M)) were synthesized by adding  $\text{Fe}_3\text{O}_4@\text{SiO}_2@\text{APTES}$  (0.5700 g), GO (0.6000 g), DCC (1.5000

g), NHS (0.2400 g) and DTPA-CS(L) or DTPA-CS(M) (0.3700 g) into DMF (50.0 mL). Mixed materials were heated up to 60.0 °C for 24 h. Temperature and time of reaction were optimized by trial. The products were rinsed with DMF and ethanol and dried at 25.0 °C for 12 h.

### Instrumentation

FT-IR spectra were obtained by the Fourier Transform Infrared spectrophotometer (FT-IR, PerkinElmer Spectrum 65). Philips PW1730 was used for having XRD patterns. The field emission scanning electron microscopy was performed by TESCAN MIRA 3. Thermal decomposition data was obtained using gravimetric analysis (TA SDT Q600, at argon atmosphere). The Meghnatis Daghigh Kavir was used for obtaining the magnetic property of the composites. N<sub>2</sub> adsorption/desorption isotherm was obtained by BEL BELSORP MINI II. The UV-Vis spectrophotometry was done using Jasco V-630.

### Modeling

In general, in multiple regression model, response ( $R$ ) can be related to  $f$  predictor variables ( $x_i$ ) with considering interaction terms according to Eq. (1):

$$R = \beta_0 + \sum_{i=1}^f \beta_i x_i + \sum_{i=1}^f \beta_{ii} x_i^2 + \sum_{i=1}^{f-1} \sum_{j=2}^f \beta_{ij} x_i x_j + \varepsilon \quad (1)$$

where,  $\beta_0$  is the intercept,  $\beta_i$  is the regression coefficient for the linear terms,  $\beta_{ii}$  corresponds to the quadratic terms and  $\beta_{ij}$  shows the interactions terms. Also,  $\varepsilon$  is a statistical error. It is assumed that error has a normal distribution.

Hypothesis testing in regression is helpful for measuring the adequacy of the model and determining the important predictors. In this regard, the null ( $H_0$ ) and alternative hypotheses ( $H_a$ ) are:

$$H_0: \beta_i = \beta_{ii} = \beta_{jj} = \beta_{ij} = 0 \quad (2)$$

$$H_a: \beta_i \neq 0 \text{ and/or } \beta_{ii} \neq 0 \text{ and/or } \beta_{ij} \neq 0$$

Rejection of  $H_0$  implies that at least one of the predictors has significant contribution to the model. To conduct hypothesis, error must have normal distribution with zero mean and constant variance.

Analysis of variance (ANOVA) is used as a test procedure for testing  $H_0$  at 95% confidence interval (with significant level of  $\alpha = 0.05$ ).  $F$  statistic is calculated by Eq. (3):

$$F_0 = \frac{SS_{\text{model}}/k}{SS_{\text{residual}}/(n-p)} \quad (3)$$

in which,  $SS_{\text{model}}$  and  $SS_{\text{residual}}$  are sum of square for model and residual, respectively,  $n$  is the number of observation,  $k$  is number of linear, quadratic and interaction terms in the model and  $p (= k+1)$  is the number of all terms including the intercept.

If  $F_0$  is greater than  $F_{\alpha,k,n-k-1}$ , then  $H_0$  is rejected. Alternatively, when the  $p$ -value of model is less than  $\alpha$ ,  $H_0$  is rejected.

There are some statistics in order to select and evaluate the adequacy of the model. Table 2 contains the formula for residual, sum of squares of residual, model and total ( $SS_{\text{residual}}$ ,  $SS_{\text{model}}$ ,  $SS_{\text{total}}$ ), prediction error sum of squares (PRESS), coefficient of determination ( $R^2$ ), adjusted coefficient of determination ( $R_{\text{Adj}}^2$ ), predicted coefficient of determination ( $R_{\text{Pred}}^2$ ), standard deviation ( $s$ ), coefficient of variation (C.V.%), adequate precision (A.P.) and root mean square error (RMSE) [33].

**Table 2** Statistic for testing the adequacy of model

Statistic	Formula
Residual	residual = $R_{\text{exp},i} - R_{\text{cal},i}$
Sum of squares of residual	$SS_{\text{residual}} = \sum_{i=1}^n (R_{\text{exp},i} - R_{\text{cal},i})^2$
Sum of squares of model	$SS_{\text{model}} = SS_{\text{total}} - SS_{\text{residual}}$
Sum of squares of total	$SS_{\text{total}} = \sum_{i=1}^n (R_{\text{exp},i} - \bar{R})^2$
Prediction error sum of squares	$PRESS = \sum_{i=1}^n (R_{\text{exp},i} - R_{\text{cal},(i)})^2$
Coefficient of determination	$R^2 = 1 - \frac{SS_{\text{residual}}}{(SS_{\text{model}} + SS_{\text{residual}})}$
Adjusted coefficient of determination	$R_{\text{Adj}}^2 = 1 - \frac{SS_{\text{residual}}/(n-p)}{(SS_{\text{model}} + SS_{\text{residual}})/(n-1)}$
Predicted coefficient of determination	$R_{\text{Pred}}^2 = 1 - \frac{PRESS}{(SS_{\text{model}} + SS_{\text{residual}})/(n-1)}$
Standard deviation	$s = \sqrt{\frac{\sum_{i=1}^n (R_{\text{exp},i} - \bar{R})^2}{n-1}}$
Coefficient of variation	$C.V. = \frac{s}{\bar{R}} \times 100\%$
Adequate precision	$A.P. = \frac{\text{Signal}}{\text{Noise}}$

Root mean square error

$$\text{RMSE} = \sqrt{\frac{\text{SS}_{\text{residual}}}{n - p}}$$

---

$R_{\text{exp},i}$  and  $R_{\text{cal},i}$  are experimental (observed) and calculated (predicted) responses, respectively. SS stands for sum of squares. Also,  $\bar{R}$  represents the mean of response and PRESS shows how well the model fits every points in the design.

---

## Design of Experiments

Central Composite Design (CCD) based on the Response Surface Methodology was used for design of experiments. The selected factors were initial pH, temperature ( $T$ ) and nanocomposite concentration ( $C_{\text{NC}}$ ). The initial concentration of BB41 was kept constant ( $C_0 = 10.0 \text{ mg}\cdot\text{L}^{-1}$ , 10.0 ml). The percentage of dye removal ( $Re\%$ ) was selected as the response of the design and obtained by Eq. (4) [34]:

$$Re\% = \frac{(C_0 - C_{\text{res.}})}{C_0} \times 100\% \quad (4)$$

where  $C_{\text{res.}}$  was the dye residual concentration.

Five levels were considered for each factor in CCD. The factorial, axial and center points were coded as “ $\pm 1$ ”, “0”, and “ $\pm\alpha$ ”, respectively. The levels of factors are presented in Table 3.

**Table 3** Levels of factors used in CCD

Factor	Level				
	$-\alpha$	-1	0	+1	$+\alpha$
pH	4.14	5.50	7.50	9.50	10.86
$T$ ( $^{\circ}\text{C}$ )	17.8	28.0	43.6	58.0	68.2
$C_{\text{NC}}$ ( $\text{g}\cdot\text{L}^{-1}$ )	0.12	0.60	1.30	2.00	2.48

Synthesized nanocomposites (NC(L) and NC(M)) were used for each set of design. Twenty experiments were carried out in order to identify the effect of factors on the response and interactions between factors along with optimum conditions. The contacting time was 60 min for all runs.

## Kinetics Experiments

The results of CCD optimization were used for kinetics and equilibrium studies. In this regard, pH and temperature of solutions were set at 9.02 and 47.1  $^{\circ}\text{C}$ , respectively. Then 0.0198 g of nanocomposite was added into the solution. Then, each mixture was shaken at 150 rpm. Initial concentration of BB41 were 8.0, 15.0, and 30.0  $\text{mg}\cdot\text{L}^{-1}$  (10.0 ml) for kinetics experiments. The residual concentration ( $C_t$ ) was obtained using the UV-Vis spectrophotometer (at  $\lambda_{\text{max}} = 608 \text{ nm}$ ) at different time intervals and the amount of BB41 adsorbed per unit mass

of nanocomposite ( $q_t$  as  $\text{mg}\cdot\text{g}^{-1}$ ) was calculated by Eq. (5) [35]:

$$q_t = \frac{V(C_0 - C_t)}{m} \quad (5)$$

in which,  $V$  was the volume of dye solution (as L) and  $m$  was the nanocomposite mass (as g).

The maximum standard deviation was calculated  $\pm 0.4 \text{ mg}\cdot\text{g}^{-1}$  for  $q_t$  by repeating the experiments three times.

### Equilibrium Experiments

Dye concentrations ranging from 50.0 to 600.0  $\text{mg}\cdot\text{L}^{-1}$  were used for doing equilibrium experiments. The amount of 0.0198 g nanocomposite was dispersed in 10.0 ml of dye solutions with pH of 9.02 and temperature of 47.1 °C. All mixtures were placed into the water bath shaker for 4 h (at 150 rpm). According to Eq. (6), the equilibrium concentrations ( $C_e$ ) were used for calculating the amount of adsorbed dye per unit mass of nanocomposite at equilibrium ( $q_e$  as  $\text{mg}\cdot\text{g}^{-1}$ ) [34]:

$$q_e = \frac{V(C_0 - C_e)}{m} \quad (6)$$

All experiments were repeated three times and the maximum standard deviation was  $\pm 3.0 \text{ mg}\cdot\text{g}^{-1}$  for  $q_e$ .

### Recovery of Nanocomposite

Recovery of adsorbent had three stages. At saturation step, the amount of 0.0200 g of nanocomposite was added into 10.0 ml BB41 solution with concentration of 300.0  $\text{mg}\cdot\text{L}^{-1}$ . The nanocomposite was separated from solution after 24 h and dried. In the second stage (desorption step), the saturated nanocomposite was washed out with 10.0 ml of different eluents including hydrochloric acid, sodium hydroxide or sodium chloride solutions (0.1  $\text{mol}\cdot\text{L}^{-1}$ ). The desorption step was repeated in the presence of ultrasonic waves for 5 min. At adsorption stage, a newly prepared solution of BB41 (10.0  $\text{mg}\cdot\text{L}^{-1}$ , 10.0 ml at pH of 9.02 and temperature of 47.1 °C) was contacted with 0.0198 g of the nanocomposite. After 10 min of adsorption, the nanocomposite was separated, dried and reused for the next cycle [36]. Seven desorption - adsorption cycles were tested.

### Results and Discussion

## Characterizations

FT-IR spectra of materials used for synthesizing NC(M) are presented in Fig. 2. NC(M) spectrum had the characteristics peak of Fe<sub>3</sub>O<sub>4</sub>, Fe<sub>3</sub>O<sub>4</sub>@SiO<sub>2</sub>, Fe<sub>3</sub>O<sub>4</sub>@SiO<sub>2</sub>@APTES, DTPA-CS(M) and GO. Relevantly, the peaks of Fe–O ( $\approx 640\text{ cm}^{-1}$ ), Si–O ( $\approx 1088\text{ cm}^{-1}$ ) and C–H (2930, and  $2852\text{ cm}^{-1}$ ) were observed. Cross-linking was resulted from amide formation and chemical bonding between DTPA-CS(M) and/or CS(M)-APTES portion of modified magnetite and/or CS(M)-GO and/or DTPA-APTES portion [37]. Correspondingly, the peak for N–H (secondary amide) was overlapped with O–H and primary amine at  $3327\text{ cm}^{-1}$  [38]. A peak at  $1575\text{ cm}^{-1}$  belonged to the N–H bending vibration and C–N (amine) had a peak at  $1245\text{ cm}^{-1}$ . The nanocomposite had aromatic C=C peaks at  $1627$  and  $1437\text{ cm}^{-1}$ . However, carbonyl vibration was too low (at  $\approx 1715\text{ cm}^{-1}$ ) due to the formation of amide [39].

**Fig. 2** FT-IR spectra of Fe<sub>3</sub>O<sub>4</sub>, Fe<sub>3</sub>O<sub>4</sub>@SiO<sub>2</sub>, Fe<sub>3</sub>O<sub>4</sub>@SiO<sub>2</sub>@APTES, GO, DTPA, CS(M), DTPA-CS(M), and NC(M)

The XRD patterns are shown in Fig. 3. The peaks of Fe<sub>3</sub>O<sub>4</sub> were observed at  $2\theta = 30.8^\circ$ ,  $36.2^\circ$ ,  $43.7^\circ$ ,  $54.1^\circ$ ,  $57.6^\circ$ , and  $63.4^\circ$  [40]. This pattern was repeated in Fe<sub>3</sub>O<sub>4</sub>@SiO<sub>2</sub>, Fe<sub>3</sub>O<sub>4</sub>@SiO<sub>2</sub>@APTES and NC(M). Also, nanocomposite had patterns of DTPA-CS(M). GO peak (at  $2\theta = 10.3^\circ$ , corresponding to the interlayer spacing of 0.81 nm) was not clearly observed in NC(M). However, the distinguished peak of GO was in XRD pattern of NC(L) in our previous study [20]. It could be concluded that lesser GO sheets were attached to the surface of NC(M) due to lesser hydrophilicity property of DTPA-CS(M) [7].

**Fig. 3** XRD patterns of Fe<sub>3</sub>O<sub>4</sub>, Fe<sub>3</sub>O<sub>4</sub>@SiO<sub>2</sub>, Fe<sub>3</sub>O<sub>4</sub>@SiO<sub>2</sub>@APTES, GO, DTPA-CS(M), and NC(M)

Fig. 4 shows FESEM images of Fe<sub>3</sub>O<sub>4</sub>, Fe<sub>3</sub>O<sub>4</sub>@SiO<sub>2</sub>, Fe<sub>3</sub>O<sub>4</sub>@SiO<sub>2</sub>@APTES, GO, DTPA-CS(M), and NC(M). Cauliflower structure was found for Fe<sub>3</sub>O<sub>4</sub>, Fe<sub>3</sub>O<sub>4</sub>@SiO<sub>2</sub>, and Fe<sub>3</sub>O<sub>4</sub>@SiO<sub>2</sub>@APTES. The average size of Fe<sub>3</sub>O<sub>4</sub> nanoparticles was 34 nm, based on the size distribution histograms (Supplementary Information, Fig. S1). Fe<sub>3</sub>O<sub>4</sub>@SiO<sub>2</sub> and Fe<sub>3</sub>O<sub>4</sub>@SiO<sub>2</sub>@APTES had the average size of 56 and 83 nm, respectively. Sheets were distinguished in FESEM image of GO. Besides, DTPA-CS(M) had polyhedron and rod structures. The morphology of NC(M) was quite complex and contained sheets, cauliflower and rod shapes similar to NC(L) [20].

**Fig. 4** FESEM images of Fe<sub>3</sub>O<sub>4</sub>, Fe<sub>3</sub>O<sub>4</sub>@SiO<sub>2</sub>, Fe<sub>3</sub>O<sub>4</sub>@SiO<sub>2</sub>@APTES, GO, DTPA-CS(M), and NC(M)

The thermal stability of Fe<sub>3</sub>O<sub>4</sub>, Fe<sub>3</sub>O<sub>4</sub>@SiO<sub>2</sub>, Fe<sub>3</sub>O<sub>4</sub>@SiO<sub>2</sub>@APTES, GO, DTPA-CS(M), and NC(M) was evaluated by thermal gravimetric analysis (TGA). The steps in TGA plot represented mass loss due to evaporation, oxidation and decomposition. The results of TGA and its first derivative (DTG) are shown in Fig. 5 (a and b). Fe<sub>3</sub>O<sub>4</sub> had a little change in mass (9.2%) in the whole range of temperature. The mass loss were 14 and 20% for Fe<sub>3</sub>O<sub>4</sub>@SiO<sub>2</sub> and Fe<sub>3</sub>O<sub>4</sub>@SiO<sub>2</sub>@APTES, respectively. The nanocomposite was approximately stable up to 254 °C being a little more stable in comparison with NC(L) which was stable up to 248 °C [20]. The first mass loss was associated to the evaporation the water adsorbed at NC(M) surface (below 100 °C). Degradation and decomposition of organic components of APTES, DTPA, deacetylation of CS(M) and losing carbon monoxide and carbon dioxide were the major reasons for mass loss of NC(M) at temperature higher than 254 °C [22, 41, 42].

**Fig. 5** (a) TGA and (b) DTG curves of Fe<sub>3</sub>O<sub>4</sub>, Fe<sub>3</sub>O<sub>4</sub>@SiO<sub>2</sub>, Fe<sub>3</sub>O<sub>4</sub>@SiO<sub>2</sub>@APTES, GO, DTPA-CS(M), and NC(M)

The magnetization plots of magnetic materials are presented in Fig. 6. The saturation magnetization of Fe<sub>3</sub>O<sub>4</sub>, Fe<sub>3</sub>O<sub>4</sub>@SiO<sub>2</sub>, Fe<sub>3</sub>O<sub>4</sub>@SiO<sub>2</sub>@APTES were 42, 34 and 29 emu·g<sup>-1</sup>, respectively. The magnetic property of NC(M) decreased dramatically to 2.5 emu·g<sup>-1</sup>. However, the value of 9.2 was obtained for NC(L) in previous study [20]. The difference between saturation magnetization of NC(M) and NC(L) showed that the layer of chitosan with more monomer of D-amino glucose caused the magnetic property declined sharply. Although this value was low for NC(M), it surprisingly had an excellent magnetic property.

**Fig. 6** Magnetization measurements for Fe<sub>3</sub>O<sub>4</sub>, Fe<sub>3</sub>O<sub>4</sub>@SiO<sub>2</sub>, Fe<sub>3</sub>O<sub>4</sub>@SiO<sub>2</sub>@APTES and NC(M)

Nitrogen adsorption/desorption isotherm at 77 K is presented in Fig. 7 (a). NC(M) showed type IV isotherm with hysteresis loops proofing that it is a mesoporous adsorbent [43]. NC(M) exhibited H3 type hysteresis loop [44]. In the type H3 loop, there was no limiting adsorption at high relative pressure ( $p/p_0$ ). It confirmed aggregation of plate-like particles associate with slit-shape pores. Estimation of pore size distribution was not reliable for type H3 loop. The Brunauer-Emmett-Teller (BET) plot is depicted in Fig. 7 (b). The specific surface area obtained by BET theory was too small (3.50 m<sup>2</sup>·g<sup>-1</sup>). Actually BET theory is just applicable for finely-divided materials not for adsorbents with heterogeneous surfaces. Thus, the BET theory was not suitable for predicting the surface area and pore size of NC(M) [44].

**Fig. 7** (a) N<sub>2</sub> adsorption/desorption isotherm at 77 K, (b) BET plot of NC(M)

## Central Composite Design and Statistical Analysis

Experiments revealed that the amount of adsorbed dye was very low when NC(M) was used. The maximum percentage of dye removal was  $\approx 31\%$  at optimum conditions. Indeed, introduction of D-amino glucose monomers decreased hydrophilicity of NC(M) resulted in repelling the hydrophilic azo dye from the surface of adsorbent [27]. However, percentage of dye removal reached 93.41% in the presence of NC(L) with higher hydrophilicity. It can be concluded that hydrophilicity had more effect on the adsorption than the number of functional groups. In This regard, the result of CCD was just reported for NC(L) (Supplementary Information, Table S1).

Least squares method was used for introducing a multiple regression model and estimating the regression coefficients ( $\beta$ ). A quadratic model was suggested by Design-Expert software according to Eq. (7):

$$\begin{aligned} Re\% = & 83.12 + 1.60pH + 6.59T + 16.06C_{NC(L)} \\ & + 0.2913pH \cdot T + 2.32pH \cdot C_{NC(L)} \\ & - 3.44T \cdot C_{NC(L)} - 0.9868pH^2 \\ & - 4.26T^2 - 8.4C_{NC(L)}^2 \end{aligned} \quad (7)$$

Fig. 8 confirms that the cumulative normal distribution of residuals is approximately a straight line implying the error ( $\varepsilon$ ) has a normal distribution [33].

**Fig. 8** Normal plot of residuals

Analysis of variance (ANOVA) for quadratic model is presented in Table 4 at 95% confidence interval.

**Table 4** Analysis of variance for quadratic model at 95% confidence interval

Source	Sum of Square	DF	Mean Square	F-value	p-value	
<b>Model</b>	3615.62	9	401.74	45.22	< 0.0001	significant
<i>pH</i>	22.42	1	22.42	2.52	0.1508	
<i>T</i>	592.76	1	592.76	66.72	< 0.0001	
<i>C<sub>NC(L)</sub></i>	2251.83	1	2251.83	253.47	< 0.0001	
<i>pH</i> · <i>T</i>	0.6788	1	0.6788	0.0764	0.7892	
<i>pH</i> · <i>C<sub>NC(L)</sub></i>	42.88	1	42.88	4.83	0.0593	
<i>T</i> · <i>C<sub>NC(L)</sub></i>	94.74	1	94.74	10.66	0.0114	
<i>pH</i> <sup>2</sup>	7.30	1	7.30	0.8221	0.3911	
<i>T</i> <sup>2</sup>	241.93	1	241.93	27.23	0.0008	
<i>C<sub>NC(L)</sub></i> <sup>2</sup>	530.51	1	530.51	59.72	< 0.0001	
<b>Residual</b>	71.07	8	8.88			
Lack of Fit	44.84	3	14.95	2.85	0.1444	not significant
Pure Error	26.23	5	5.25			
<b>Corrected Total</b>	3686.69	17				

As can be seen, the  $p$ -value were greater than 0.05 for terms of  $pH$ ,  $pH \cdot T$  and  $pH^2$  which implied that they were not significant in the model. However, the term of  $pH \cdot C_{NC(L)}$  had little effect on the response. As well, the  $p$ -value for Lack of fit (= 0.1444) showed that the model was adequate to predict the experimental data.

Results of statistic for testing the adequacy of model are summarized in Table 5.

**Table 5** Results of statistic for testing the adequacy of model

PRESS	$R^2$	$R_{Adj.}^2$	$R_{Pred.}^2$	$s$	C.V.	RMSE
818.26	0.9807	0.9590	0.7780	2.98	3.94	2.9806

Difference between  $R_{Pred.}^2$  and  $R_{Adj.}^2$  was less than 0.2 which was reasonable. Since adequate precision (ratio of signal to noise) was greater than 4, the ratio was desirable. In this regard, the predicted values of response were consistent with observed results (Supplementary Information, Table S1). The values of the predicted response versus observed response is plotted in Fig. 9. As can be seen, the points lay along a straight line. This line was obtained by the least squares method.

**Fig. 9** Plot of predicted response versus observed response

### **Influence of Nanocomposite Concentration-Initial pH on the Percentage of Dye Removal**

Central Composite Design gives opportunity to study the influence of variables on the response and obtain mutual interactions [45]. The 3D response surface plot for percentage of dye removal versus nanocomposite concentration and initial pH is depicted in Fig. 10. High levels of variables had positive influence on the response.

**Fig. 10** Response surface plot for percentage of dye removal as a function of nanocomposite concentration and initial pH at temperature of 43.0 °C

The interaction between  $C_{NC(L)}$  and pH was studied by plotting interaction graph in Fig. 11. When the level of nanocomposite dosage was low ( $0.6 \text{ g} \cdot \text{L}^{-1}$ ), there was no significant changes in response at any pHs. On the contrary, an increase in concentration ( $2.0 \text{ g} \cdot \text{L}^{-1}$ ) led to higher percentage of dye removal in the whole range of pH. Furthermore, the effect of alkaline medium was considerable when  $C_{NC(L)}$  increased. For example, when pH was 5.50, the increase in the concentration resulted in a 27.7% growth in  $Re\%$ . However, the growth of  $Re\%$  was 36.7% at pH of 9.50. Point of zero charge pH ( $pH_{pzc}$ ) was 3.9 for NC(L) [20] and the charge of adsorbent

was negative at pHs greater than  $pH_{pzc}$ . At high pHs, anions of carboxylate ( $-COO^-$ ) and hydroxyl ( $OH^-$ ) were produced on the surface of NC(L). Thus, there was an electrostatic attraction between active sites of adsorbent and cationic dye molecules [46]. Relevantly, more anions were accessible when the concentration increased [47].

**Fig. 11** Percentage of dye removal versus pH at two different nanocomposite concentrations with 95% confidence interval and temperature of 43.0 °C

### **Influence of Nanocomposite Concentration-Temperature on the Percentage of Dye Removal**

Fig. 12 shows the influence of nanocomposite concentration and temperature on the percentage of BB41 removal. By following the variations, it was concluded that the adsorption was endothermic and higher temperature was in favor of adsorption [22]. It implied that the adsorption process was controlled by the dye diffusion into the surface and pores of nanocomposite [48]. Dye removal increased when the concentration of NC(L) increased. The surface of nanocomposite is covered by different functional groups such as carboxyl, hydroxyl, amine and aromatic rings. When more functional groups were available (as a result of increased concentration), more interactions including electrostatic interaction, hydrogen bonding, cation- $\pi$  and  $\pi$ - $\pi$  stacking between dye and adsorbent were possible. The interaction plot (Fig. 13) confirms that higher efficiency of adsorption needs elevated temperature and concentration. At low level of temperature (28.0 °C), the percentage of dye removal was 44.4% at concentration of 0.6  $g \cdot L^{-1}$  and  $Re\%$  reached 83.4% at 2.0  $g \cdot L^{-1}$ . However, at  $T = 58.0$  °C, the difference between  $Re\%$  was 31.8% when concentration changed from 0.6 to 2.0  $g \cdot L^{-1}$ .

**Fig. 12** Response surface plot for percentage of dye removal as a function of nanocomposite concentration and temperature at pH of 7.50

**Fig. 13** Percentage of dye removal versus temperature at two different nanocomposite concentrations with 95% confidence interval and pH of 7.50

### **Influence of Initial pH-Temperature on the Percentage of Dye Removal**

The impact of pH-temperature on the dye removal efficiency is illustrated in Fig. 14. The percentage of BB41 removal was not significantly changed by increasing the initial pH. However, rising temperature led to higher adsorption and  $Re\%$ . For instance,  $Re\%$  changed from 72.2% (at 28.0 °C) to 85.4% (at 58.0 °C) by rising temperature. Fig. 15 clearly presents the interaction between pH and temperature. The adsorption was not affected too much by pH

at constant temperature. However, warmer solution led to more dye adsorption at a specific pH [49]. It could be interpreted that more facile diffusion was possible at higher temperature [48].

**Fig. 14** Response surface plot for percentage of dye removal as a function of pH and temperature at nanocomposite concentration of  $1.30 \text{ g}\cdot\text{L}^{-1}$

**Fig. 15** Percentage of dye removal versus pH at two temperatures with 95% confidence interval and nanocomposite concentration of  $1.30 \text{ g}\cdot\text{L}^{-1}$

## Optimization and Adsorption Mechanism

Finding the conditions in which the process is optimized is one the important challenges in the industries. By using analytical and mathematical techniques, numerical optimization was done [45]. In this regard, maximum *Re%* was calculated 93.4% when pH was 9.02 at temperature of  $47.1 \text{ }^\circ\text{C}$  and nanocomposite concentration of  $1.98 \text{ g}\cdot\text{L}^{-1}$ . The experimental result of *Re%* was 95.4% which was consistent with the calculated value (93.4%).

Percentage of BB41 removal is reported in Table 6 when CS(L), DTPA-CS(L), GO and NC(L) were used as the adsorbent at optimum conditions. The data confirmed that there was a synergism effect when different functional groups were attached to the surface of the NC(L). The active groups were carboxyl (originated from GO and DTPA), hydroxyl (originated from APTES, GO and CS(L)), amine (in the CS(L) structure) and aromatic rings (in the GO sheets). Thus, the possible adsorption mechanisms could be electrostatic interactions between functional groups of NC(L) and cationic dye. When pH was much greater than  $\text{pH}_{\text{pzc}}$ , the carboxyl and hydroxyl groups were negative in the surface of adsorbent resulted in the attracting BB41 [50]. Besides, there were cation- $\pi$  interactions as a noncovalent bonding between cationic dye and  $\pi$  system, along with  $\pi$ - $\pi$  stacking resulted from  $\pi$  electrons in the aromatic portions of BB41 and conjugated aromatic rings of GO [18]. H-bonding could serve as other factors in adsorption mechanism [51].

**Table 6** Percentage of BB41 removal using ingredients and NC(L) at optimum conditions

<b>Adsorbent</b>	<b><i>Re %</i></b>
CS(L)	36.0
DTPA-CS(L)	52.0
GO	81.4
NC(L)	95.4

## Kinetics Adsorption Studies

In order to design an adsorption reactor, it is crucial to obtain the constant of adsorption

rate. In this regard, the uptake rate of dye is studied at optimum conditions (pH of 9.02, temperature of 47.1 °C and NC(L) concentration of 1.98 g·L<sup>-1</sup>). The results of kinetics studies are presented in Fig. 16, Fig. 17 and Fig. 18 for concentration of 8.0 mg·L<sup>-1</sup>, 15.0 mg·L<sup>-1</sup> and 30.0 mg·L<sup>-1</sup>, respectively.

**Fig. 16** Experimental and fitted kinetics data for adsorption of BB41 with concentration of 8.0 mg·L<sup>-1</sup> under optimum conditions

**Fig. 17** Experimental and fitted kinetics data for adsorption of BB41 with concentration of 15.0 mg·L<sup>-1</sup> under optimum conditions

**Fig. 18** Experimental and fitted kinetics data for adsorption of BB41 with concentration of 30.0 mg·L<sup>-1</sup> under optimum conditions

For all concentrations, the dye adsorption was quite fast. For example, about 65.93% of dye with the initial concentration of 8.0 mg·L<sup>-1</sup> was removed within the first 20 min. The percentage of BB41 removal was 61.49 and 47.15% after 20 min when the initial concentrations were 15.0 and 30.0 mg·L<sup>-1</sup>, respectively. The dye removal was followed by a mild-slope adsorption and equilibrium was achieved at 30 min. Some kinetics models were listed in Table 7 and used for fitting the experimental data.

**Table 7** Different kinetics models used for fitting the experimental data

Kinetics model	Equation	Reference
<b>Two parameters models</b>		
Pseudo-first-order (PFO)	$q_t = q_e(1 - \exp(-k_1 t))$	[52]
Pseudo-second-order (PSO)	$q_t = q_e^2 k_2 t / (1 + q_e k_2 t)$	[53]
Elovich	$q_t = (1/b_E) \ln(1 + a_E b_E t)$	[54]
<b>Three parameters models</b>		
Mixed 1, 2-order (MOE)	$q_t = q_e(1 - \exp(-k_1 t)) / (1 - F_2 \exp(-k_1 t))$	[55]
Pseudo-n-order (PnO)	$q_t = q_e - ((n - 1)k_1 t + q_e^{1-n})^{\frac{1}{1-n}}$	[56]
Modified pseudo-n-order (MPnO)	$q_t = q_e(1 - \exp(-nk_1 t))^{\frac{1}{n}}$	[57]
Fractal-like pseudo-first-order (FL-PSO)	$q_t = q_e(1 - \exp(-k_1' t^\alpha))$	[58]
Fractal-like pseudo-second-order (FL-PSO)	$q_t = q_e^2 k_2' t^\alpha / (1 + q_e k_2' t^\alpha)$	[59]

The adequacy of the models was checked by  $R_{Adj}^2$ , corrected Akaike information criterion ( $AIC_c$ ), chi-square ( $\chi^2$ ) and RMSE. The  $AIC_c$  and  $\chi^2$  were calculated by the following equations, respectively [60, 61]:

$$AIC_c = 1 + \ln\left(\frac{SS_{residual}}{n}\right) + \frac{2(p + 1)}{n - p - 2} \quad (8)$$

$$\chi^2 = \sum_{i=1}^n \frac{(q_{\text{exp},i} - q_{\text{cal},i})^2}{q_{\text{cal},i}} \quad (9)$$

in which,  $n$  was the number of experimental data and  $p$  was the parameters number.

The parameters and goodness of fit for each model were obtained by non-linear regression. The results are presented in Table 8.

**Table 8** Model parameters along with  $R_{\text{Adj.}}^2$ ,  $\text{AIC}_c$ ,  $\chi^2$  and RMSE obtained by non-linear regression

Model	$C_0$ (mg · L <sup>-1</sup> )	Parameter			Goodness of Fit			
<b>PFO</b>		$q_e$ (mg · g <sup>-1</sup> )	$k_1$	-	$R_{\text{Adj.}}^2$	$\text{AIC}_c$	$\chi^2$	RMSE
	8.0	2.77	0.101		0.9901	-2.7915	0.0688	0.1082
	15.0	6.16	0.073		0.9927	-1.5455	0.2834	0.2017
	30.0	9.27	0.131		0.9743	0.4419	1.0059	0.5448
<b>PSO</b>		$q_e$ (mg · g <sup>-1</sup> )	$k_2$	-	$R_{\text{Adj.}}^2$	$\text{AIC}_c$	$\chi^2$	RMSE
	8.0	3.24	0.035		0.9898	-2.7631	0.0952	0.1097
	15.0	7.40	0.011		0.9954	-2.0073	0.1394	0.1601
	30.0	10.50	0.015		0.9944	-1.0834	0.2491	0.2541
<b>Elovich</b>		$a_E$	$b_E$	-	$R_{\text{Adj.}}^2$	$\text{AIC}_c$	$\chi^2$	RMSE
	8.0	0.592	1.36		0.9653	-1.5407	0.2766	0.2022
	15.0	0.842	0.548		0.9824	-0.6610	0.2697	0.3139
	30.0	3.524	0.478		0.9872	-0.2588	0.1681	0.3838
<b>MOE</b>		$q_e$ (mg · g <sup>-1</sup> )	$k_1$	$F_2$	$R_{\text{Adj.}}^2$	$\text{AIC}_c$	$\chi^2$	RMSE
	8.0	2.85	0.058	0.49	0.9918	-2.6193	0.0666	0.0986
	15.0	11.47	0.040	1.78	0.9962	-1.8237	0.1459	0.1467
	30.0	10.50	0.000	1.00	0.9937	-0.6072	0.2491	0.2541
<b>PnO</b>		$q_e$ (mg · g <sup>-1</sup> )	$k_1$	$n$	$R_{\text{Adj.}}^2$	$\text{AIC}_c$	$\chi^2$	RMSE
	8.0	2.89	0.076	1.34	0.9919	-2.6352	0.0629	0.0978
	15.0	6.70	0.029	1.51	0.9958	-1.7440	0.1528	0.1527
	30.0	11.87	0.002	2.78	0.9951	-0.8557	0.1395	0.2380
<b>MPnO</b>		$q_e$ (mg · g <sup>-1</sup> )	$k'$	$n$	$R_{\text{Adj.}}^2$	$\text{AIC}_c$	$\chi^2$	RMSE
	8.0	2.80	0.083	1.10	0.9928	-2.7438	0.0629	0.0926
	15.0	6.28	0.045	1.23	0.9982	-2.5805	0.0771	0.1005
	30.0	9.81	0.030	1.83	0.9994	-3.0175	0.0112	0.0808
<b>FL-PFO</b>		$q_e$ (mg · g <sup>-1</sup> )	$k'_1$	$a$	$R_{\text{Adj.}}^2$	$\text{AIC}_c$	$\chi^2$	RMSE
	8.0	2.82	0.119	0.90	0.9907	-2.4958	0.0778	0.1048
	15.0	6.31	0.093	0.87	0.9981	-2.5451	0.0889	0.1023
	30.0	10.00	0.209	0.67	0.9990	-2.4440	0.0202	0.1076
<b>FL-PSO</b>		$q_e$ (mg · g <sup>-1</sup> )	$k'_2$	$a$	$R_{\text{Adj.}}^2$	$\text{AIC}_c$	$\chi^2$	RMSE
	8.0	3.00	0.029	1.23	0.9926	-2.7248	0.0466	0.0935
	15.0	7.14	0.010	1.07	0.9953	-1.6285	0.1813	0.1618
	30.0	11.31	0.016	0.83	0.9968	-1.2797	0.0641	0.1926

The best model to describe the adsorption rate of BB41 was MPnO kinetics model which had  $R_{\text{Adj.}}^2$  close to unity, lesser  $\text{AIC}_c$ ,  $\chi^2$  and RMSE.

Many steps are involved in the adsorption process such as external mass transfer of dye from the bulk of solution, film diffusion and internal diffusion of dye into the composite sites, and eventually the adsorption itself [62]. Weber and Morris showed [63] that if the intra-particle

diffusion stage was the main rate-limiting step, the plot of  $q_t$  versus  $t^{0.5}$  could be linear passing through the origin according to Eq. (10):

$$q_t = K_{\text{dif}}t^{0.5} + C \quad (10)$$

where,  $K_{\text{dif}}$  was to the intra-particle diffusion rate constant and  $C$  was the intercept.

However, a multi-linear plot indicates that the adsorption process is divided into different steps [64]. The profile presented in Fig. 19 has two linear segments. This kind of variation implied that there was an immediate and external surface adsorption at stage (I) followed by a gradual sorption at stage (II). Indeed, the process was controlled by film diffusion at stage (I) and the line with the lower slope (stage (II)) was attributed to the lower adsorption rate and intra-particle diffusion was the rate limiting step [65, 66].

**Fig. 19** Intra-particle diffusion plot for BB41 adsorption at different concentrations under optimum conditions

## Equilibrium Adsorption Results

The distribution of BB41 between solution and NC(L) can be demonstrated by isotherms at equilibrium. The experimental results were fitted by different isotherms. The most common adsorption isotherms are listed in Table 9.

**Table 9** Different isotherms used for fitting the experimental data

Isotherm	Equation	Reference
<b>Two parameters models</b>		
Langmuir	$q_e = q_m K_L C_e / (1 + K_L C_e)$	[67]
Freundlich	$q_e = K_F C_e^c$	[68]
Temkin	$q_e = (RT/b_T) \ln(K_T C_e)$	[69]
Modified Langmuir	$q_e = q_m K_{ML} C_e / ((C_s - C_e) + K_{ML} C_e)$	[70]
<b>Three parameters models</b>		
Redlich-Peterson	$q_e = K_{RP} C_e / (1 + \alpha_{RP} C_e^\beta)$	[71]
Toth	$q_e = q_m a_T C_e / (1 + (a_T C_e)^c)^{1/c}$	[72]
Extended Langmuir	$q_e = q_m K_{EL} C_e / (1 + K_{EL} C_e + (a(K_{EL} C_e)^{1/2}))$	[73]
Langmuir-Freundlich	$q_e = (q_m (K_{LF} C_e)^c) / (1 + (K_{LF} C_e)^c)$	[74]
Modified Langmuir-Freundlich	$q_e = q_m (K_{MLF} C_e)^c / ((C_s - C_e)^c - (K_{MLF} C_e)^c)$	[70]

The adsorption isotherms for BB41 on NC(L) are depicted in Fig. 20. An increase in adsorption capacity was observed as the equilibrium concentration of dye increased until NC(L) was saturated.

**Fig. 20** Adsorption isotherms for adsorption of BB41 under optimum conditions

The parameters and goodness of fit are presented in Table 10.

**Table 10** Isotherm parameters along with  $R_{Adj}^2$ ,  $AIC_c$ ,  $\chi^2$  and RMSE obtained by non-linear regression

Isotherm	Parameter			Goodness of Fit			
Langmuir	$q_m$ (mg · g <sup>-1</sup> )	$K_L$	-	$R_{Adj}^2$	$AIC_c$	$\chi^2$	RMSE
	46.48	-1261773		0.6712	6.3854	17.2714	1.1070
Freundlich	$K_F$	$c$	-	$R_{Adj}^2$	$AIC_c$	$\chi^2$	RMSE
	19.15	0.17		0.9702	3.8496	1.5797	2.8190
Temkin	$b_T$	$K_T$	-	$R_{Adj}^2$	$AIC_c$	$\chi^2$	RMSE
	351.17	2.72		0.9897	3.0393	0.6220	2.0098
Modified Langmuir	$q_m$ (mg · g <sup>-1</sup> )	$K_{ML}$	-	$R_{Adj}^2$	$AIC_c$	$\chi^2$	RMSE
	46.48	-890953		0.6712	6.3856	17.2743	10.0180
Redlich-Peterson	$K_{RP}$	$a_{RP}$	$\beta$	$R_{Adj}^2$	$AIC_c$	$\chi^2$	RMSE
	11390440	594921	0.83	0.9702	4.4496	1.5797	2.8119
Toth	$q_m$ (mg · g <sup>-1</sup> )	$a_T$	$c$	$R_{Adj}^2$	$AIC_c$	$\chi^2$	RMSE
	63.53	0.18	0.54	0.9954	2.5808	0.2265	1.1838
Extended Langmuir	$q_m$ (mg · g <sup>-1</sup> )	$K_{EL}$	$a$	$R_{Adj}^2$	$AIC_c$	$\chi^2$	RMSE
	64.63	0.18	1.66	0.9953	2.5981	0.2270	1.1941
Langmuir-Freundlich	$q_m$ (mg · g <sup>-1</sup> )	$K_{LF}$	$c$	$R_{Adj}^2$	$AIC_c$	$\chi^2$	RMSE
	61.88	0.045	0.64	0.9958	2.4956	0.2063	1.1345
Modified Langmuir-Freundlich	$q_m$ (mg · g <sup>-1</sup> )	$K_{MLF}$	$c$	$R_{Adj}^2$	$AIC_c$	$\chi^2$	RMSE
	55.87	41.77	0.70	0.9972	2.0713	0.1469	0.9176

Among models, the modified Langmuir-Freundlich isotherm was the best one to fit the experimental data. This equation takes into account the heterogeneity of the adsorbent surface which is in agreement with the structure of NC(L) [70]. The maximum capacity of adsorbent was calculated 55.87 mg · g<sup>-1</sup> which was comparable with other investigations [75, 76]. Table 11 represents the amount of  $q_m$  obtained by different adsorbents for BB41 removal.

**Table 11** Comparing the maximum adsorption capacity of adsorbent used for BB41 removal

Adsorbent	$T$ (°C)	$q_m$ (mg · g <sup>-1</sup> )	Reference
Biochar derived from bio-wastes of rice husk	35	17.60	[75]
Saccharomyces cerevisiae	20	23.5	[76]
Dispersed carbon particles	25	41.40	[35]
Pistachio shell	50	41.77	[49]
Titanium (IV) oxide/calcium alginate	20	141.92	[77]
Zeolite tuff	50	192.31	[78]
NC(L)	47.1	55.87	Present work

The synthesized NC(L) had reasonable maximum adsorption capacity and was able to adsorb dye in 30 min. Also, adsorbent with magnetic property was separated from treated solution within a few seconds.

### Cyclic Regeneration of Adsorbent

Not only are the value of maximum dye uptake and the rate of adsorption important but also, adsorbent recovery is crucial for scale-up purposes. The experiments showed that the

acidic medium associated with ultrasonic waves caused to achieve a desirable desorption. Actually, the adsorbent was protonated in acid solution and BB41 was desorbed from the surface of NC(L) [36]. A facile desorption was obtained using ultrasonic waves since waves weakened the interaction between adsorbent and BB41. Fig. 21 shows the percentage of dye removal ( $Re\%$ ) after recovery cycles. The desorption-adsorption cycle was repeated seven times and the efficiency of NC(L) decreased only 12%.

**Fig. 21** Percentage of dye removal after recovery

## Conclusions

In this study, the effect of molecular weight of chitosan on the efficiency of nano-magnetic inorganic-organic adsorbents was studied. The silica-modified magnetite nanoparticles were treated with medium-molecular weight chitosan, graphene oxide and diethylenetriaminepentaacetic acid. Techniques including FT-IR, XRD, FESEM, TGA/DTG, VSM and nitrogen adsorption/desorption isotherm were applied for characterization of adsorbent (NC(M)). The adsorption behavior of synthesized nanocomposite was compared with as-prepared adsorbent containing low-molecular weight chitosan (NC(L)). NC(L) was a better adsorbent due to having more hydrophilic property and the basic blue 41 was successfully removed from aqueous solutions. Central Composite Design based on the response surface methodology was used for investigating the effective parameters on the adsorption and obtaining the optimum conditions. The maximum dye removal was achieved at pH of 9.02, temperature of 47.1 °C and NC(L) concentration of 1.98 g·L<sup>-1</sup>. H-bonding, coulombic attraction and pi-stacking interactions were the major factors of adsorption. The dye adsorption was completed within 30 min at optimum conditions. The film and intra-particle diffusions were rate-limiting steps sequentially. The modified pseudo-n-order equation was the best kinetics model to recreate the kinetics data. The equilibrium experimental data were fitted by modified Langmuir-Freundlich isotherm and the maximum adsorption capacity was 55.87 mg·g<sup>-1</sup>. Due to the physisorption of dye, the acidic medium associated with ultrasound caused the adsorbent to recover even after seven cycles.

## Acknowledgments

The authors would like to thank Bu-Ali Sina University for supporting this work.

## Declarations

**Funding** The research leading to these results received funding from Bu-Ali Sina University.

**Conflicts of interest** The authors declare that there is no conflict of interest.

**Availability of data and material** All data and materials as well as software application support published claims and comply with field standards.

**Authors' contributions** Simin Asadabadi: Conceptualization, Methodology, Funding acquisition, Project administration, Writing-original draft, Writing-review & editing. Masouma Mirzai: Investigation, Validation, Writing-original draft.

**Ethics approval** It is declared that this manuscript is containing original research, and has not been published in any journal, and is not being simultaneously considered for publication elsewhere. Submission of this paper has been made with full responsibility, based on the journal requirements, and there are no plagiarism and concerns about animal or human experimentation. The manuscript has been approved by authors who have significantly contributed and agreed with its submission to Journal of Polymers and the Environment.

**Electronic supplementary information** Electronic supplementary information associated with this article can be found in the online version. All data generated or analyzed during this study are included in supplementary information files.

## References

1. Punia P, Bharti MK, Chalia S, Dhar R, Ravelo B, Thakur P, Thakur A (2021) Recent advances in synthesis, characterization, and applications of nanoparticles for contaminated water treatment- A review. *Ceram Int* 47:1526–1550. <https://doi.org/10.1016/j.ceramint.2020.09.050>
2. Leonel AG, Mansur AAP, Mansur HS (2021) Advanced functional nanostructures based on magnetic iron oxide nanomaterials for water remediation: A review. *Water Res* 190:116693–116719. <https://doi.org/10.1016/j.watres.2020.116693>
3. Rauf MA, Meetani MA, Hisaindee S (2011) An overview on the photocatalytic degradation of azo dyes in the presence of TiO<sub>2</sub> doped with selective transition metals. *Desalination* 276:13–27. <https://doi.org/10.1016/j.desal.2011.03.071>
4. Abou Taleb MF, Abou El Fadl FI, Albalwi H (2021) Adsorption of toxic dye in wastewater onto magnetic NVP/CS nanocomposite hydrogels synthesized using gamma radiation. *Sep Purif Technol* 266:118551–118560. <https://doi.org/10.1016/j.seppur.2021.118551>
5. Khalid A, Arshad M, Crowley D (2010) *Biodegradation of Azo Dyes*. Springer Berlin Heidelberg
6. Patel H, Vashi RT (2015) *Characterization and Treatment of Textile Wastewater*. Elsevier Science, Waltham
7. Hasan M, Reza G, Massoumi B, Baghban A, Saraei M (2018) Ionically crosslinked magnetic chitosan/ $\kappa$ -carrageenan bioadsorbents for removal of anionic eriochrome black-T. *Int J Biol Macromol* 113:361–375. <https://doi.org/10.1016/j.ijbiomac.2018.02.102>
8. Panda SK, Aggarwal I, Kumar H, Prasad L, Kumar A, Sharma A, Vo D-VN, Van Thuan D, Mishra V (2021) Magnetite nanoparticles as sorbents for dye removal: A review. *Environ Chem Lett* 19:2487–2525. <https://doi.org/10.1007/s10311-020-01173-9>
9. Kadhom M, Albayati N, Alalwan H, Al-furaiji M (2020) Removal of dyes by agricultural waste. *Sustain Chem Pharm* 16:100259–100267. <https://doi.org/10.1016/j.scp.2020.100259>
10. Ramesh P, Padmanabhan V, Saravanan P, Thillainayagam BP (2021) Batch studies of turquoise blue dye (TB) adsorption onto activated carbon prepared from low-cost adsorbents: an ANN approach. *Biomass Convers Biorefin*. <https://doi.org/10.1007/s13399-021-01355-7>
11. Jazzar A, Alamri H, Malajati Y, Mahfouz R, Bouhrara M, Fihri A (2021) Recent advances in the synthesis

- and applications of magnetic polymer nanocomposites. *J Ind Eng Chem* 99:1–18. <https://doi.org/10.1016/j.jiec.2021.04.011>
12. Tamer Y, Özeren MD, Berber H (2021) High adsorption performance of graphene oxide doped double network hydrogels for removal of azo dyes from water and their kinetics. *J Polym Environ*. <https://doi.org/10.1007/s10924-021-02162-x>
  13. Bello K, Sarojini BK, Narayana B (2019) Design and fabrication of environmentally benign cellulose based hydrogel matrix for selective adsorption of toxic dyes from industrial effluvia. *J Polym Res* 26:62–74. <https://doi.org/10.1007/s10965-019-1724-6>
  14. Saheed IO, Oh W Da, Suah FBM (2021) Chitosan modifications for adsorption of pollutants – A review. *J Hazard Mater* 408:124889–124904. <https://doi.org/10.1016/j.jhazmat.2020.124889>
  15. Rastgardani M, Zolgharnein J (2021) Simultaneous determination and optimization of titan yellow and reactive blue 4 dyes removal using chitosan@hydroxyapatite nanocomposites. *J Polym Environ* 29:1789–1807. <https://doi.org/10.1007/s10924-020-01982-7>
  16. Vakili M, Qiu W, Cagnetta G, Huang J, Yu G (2021) Solvent-free mechanochemical mild oxidation method to enhance adsorption properties of chitosan. *Front Environ Sci Eng* 15:128–141. <https://doi.org/10.1007/s11783-021-1416-4>
  17. Chen A, Chen S (2009) Biosorption of azo dyes from aqueous solution by glutaraldehyde-crosslinked chitosans. *J Hazard Mater* 172:1111–1121. <https://doi.org/10.1016/j.jhazmat.2009.07.104>
  18. Jiang X, Pan W, Xiong Z, Zhang Y, Zhao L (2021) Facile synthesis of layer-by-layer decorated graphene oxide based magnetic nanocomposites for  $\beta$ -agonists/dyes adsorption removal and bacterial inactivation in wastewater. *J Alloys Compd* 870:159414. <https://doi.org/10.1016/j.jallcom.2021.159414>
  19. Huang L, Li D, Zhang D, Peng H, Ren Y (2020) Facile preparation of taurine modified magnetic chitosan nanocomposites as biodegradable adsorbents toward methylene blue. *Environ Technol* 1–14. <https://doi.org/10.1080/09593330.2020.1725140>
  20. Asadabadi S, Merati Z (2021) A tailored magnetic composite synthesized by graphene oxide, chitosan and aminopolycarboxylic acid for diminishing dye contaminant. *Cellulose* 28:2327–2351. <https://doi.org/10.1007/s10570-020-03623-7>
  21. Usman M, Ahmed A, Yu B, Wang S, Shen Y, Cong H (2021) Simultaneous adsorption of heavy metals and organic dyes by  $\beta$ -cyclodextrin-chitosan based cross-linked adsorbent. *Carbohydr Polym* 255:117486. <https://doi.org/10.1016/j.carbpol.2020.117486>
  22. Chen B, Zhao H, Chen S, Long F, Huang B, Yang B, Pan X (2019) A magnetically recyclable chitosan composite adsorbent functionalized with EDTA for simultaneous capture of anionic dye and heavy metals in complex wastewater. *Chem Eng J* 356:69–80. <https://doi.org/10.1016/j.cej.2018.08.222>
  23. Jin Z, Wang X, Sun Y, Ai Y, Wang X (2015) Adsorption of 4-n-nonylphenol and bisphenol-A on magnetic reduced graphene oxides: A combined experimental and theoretical studies. *Environ Sci Technol* 49:9168–9175. <https://doi.org/10.1021/acs.est.5b02022>
  24. Mittal H, Al A, Morajkar PP, Alhassan SM (2021) GO crosslinked hydrogel nanocomposites of chitosan/carboxymethyl cellulose – A versatile adsorbent for the treatment of dyes contaminated wastewater. *Int J Biol Macromol* 167:1248–1261. <https://doi.org/10.1016/j.ijbiomac.2020.11.079>
  25. Patil RM, Shete PB, Thorat ND, Otari S V, Barick KC, Prasad A, Ningthoujam RS, Tiwale BM, Pawar SH (2014) Superparamagnetic iron oxide/chitosan core/shells for hyperthermia application: Improved colloidal stability and biocompatibility. *J Magn Magn Mater* 355:22–30. <https://doi.org/10.1016/j.jmmm.2013.11.033>
  26. Huang X, Zhan X, Wen C, Xu F, Luo L (2018) Amino-functionalized magnetic bacterial cellulose/activated carbon composite for  $Pb^{2+}$  and methyl orange sorption from aqueous solution. *J Mater Sci Technol* 34:855–863. <https://doi.org/10.1016/j.jmst.2017.03.013>
  27. Liu Y, Zheng H, Han Y, Wu Y, Wang Y, Liu Y, Feng L (2021) Amphiphilic magnetic copolymer for enhanced removal of anionic dyes: Fabrication, application and adsorption mechanism. *Colloids Surf A* 623:126674–126688. <https://doi.org/10.1016/j.colsurfa.2021.126674>
  28. Kaemkit C, Monvisade P, Siriphannon P, Nukeaw J (2013) Water-soluble chitosan intercalated montmorillonite nanocomposites for removal of basic blue 66 and basic yellow 1 from aqueous solution. *J Appl Polym Sci* 128:879–887. <https://doi.org/10.1002/app.38255>
  29. Qu S, Yang H, Ren D, Kan S, Zou G, Li D, Li M (1999) Magnetite nanoparticles prepared by precipitation from partially reduced ferric chloride aqueous solutions. *J Colloid Interface Sci* 215:190–192. <https://doi.org/10.1006/jcis.1999.6185>
  30. Zhou L, Pan S, Chen X, Zhao Y, Zou B, Jin M (2014) Kinetics and thermodynamics studies of pentachlorophenol adsorption on covalently functionalized  $Fe_3O_4@SiO_2$ -MWCNTs core-shell magnetic microspheres. *Chem Eng J* 257:10–19. <https://doi.org/10.1016/j.cej.2014.07.060>
  31. Zolfigol MA, Ayazi-Nasrabadi R, Bagheri S, Khakyzadeh V, Azizian S (2016) Applications of a novel nano magnetic catalyst in the synthesis of 1,8-dioxo-octahydroanthene and dihydropyran[2,3-c]pyrazole

- derivatives. *J Mol Catal A Chem* 418:54–67. <https://doi.org/10.1016/j.molcata.2016.03.027>
32. Marcano DC, Kosynkin D V, Berlin JM, Sinitskii A, Sun Z, Slesarev A, Alemany LB, Lu W, Tour JM (2010) Improved synthesis of graphene oxide. *ACS Nano* 4:4806–4814. <https://doi.org/10.1021/nn1006368>
  33. Montgomery DC, Peck EA, Vining GG (2013) *Introduction to Linear Regression Analysis*. Wiley, New Jersey
  34. Bakhtiari N, Azizian S (2018) Nanoporous carbon derived from MOF-5: A superadsorbent for copper ions. *ACS Omega* 3:16954–16959. <https://doi.org/10.1021/acsomega.8b02278>
  35. Seifikar F, Azizian S (2019) A facile method for precipitating of dispersed carbon particles prepared by microwave heating and its application for dye removal. *J Mol Liq* 275:394–401. <https://doi.org/10.1016/j.molliq.2018.11.086>
  36. Zhang H, Dang Q, Liu C, Yu D, Wang Y, Pu X, Liu Y, Liang Y, Cha D (2019) Fabrication of methyl acrylate and tetraethylenepentamine grafted magnetic chitosan microparticles for capture of Cd(II) from aqueous solutions. *J Hazard Mater* 366:346–357. <https://doi.org/10.1016/j.jhazmat.2018.12.006>
  37. McMurry JE (2010) *Fundamentals of Organic Chemistry*. Cengage Learning, Belmont
  38. Zahiri Oghani F, Tahvildari K, Nozari M (2021) Novel antibacterial food packaging based on chitosan loaded ZnO nano particles prepared by green synthesis from nettle leaf extract. *J Inorg Organomet Polym* 31:43–54. <https://doi.org/10.1007/s10904-020-01621-7>
  39. Pavia DL, Lampman GM, Kriz GS (2015) *Introduction to Spectroscopy*. Cengage Learning, Belmont
  40. Sundar S, Mariappan R, Piraman S (2014) Synthesis and characterization of amine modified magnetite nanoparticles as carriers of curcumin-anticancer drug. *Powder Technol* 266:321–328. <https://doi.org/10.1016/j.powtec.2014.06.033>
  41. Bhatt R, Sreedhar B, Padmaja P (2015) Adsorption of chromium from aqueous solutions using crosslinked chitosan–diethylenetriaminepentaacetic acid. *Int J Biol Macromol* 74:458–466. <https://doi.org/10.1016/j.ijbiomac.2014.12.041>
  42. Nekouei Marnani N, Shahbazi A (2019) A novel environmental-friendly nanobiocomposite synthesis by EDTA and chitosan functionalized magnetic graphene oxide for high removal of Rhodamine B: Adsorption mechanism and separation property. *Chemosphere* 218:715–725. <https://doi.org/10.1016/j.chemosphere.2018.11.109>
  43. Wu Z, Zhong H, Yuan X, Wang H, Wang L, Chen X, Zeng G, Wu Y (2014) Adsorptive removal of methylene blue by rhamnolipid-functionalized graphene oxide from wastewater. *Water Res* 67:330–344. <https://doi.org/10.1016/j.watres.2014.09.026>
  44. Sing KSW, Everett DH, Haul RAW, Moscou L, Pierotti RA, Rouquerol J, Siemieniowska T (1982) Reporting physisorption data for gas/solid systems. *Pure Appl Chem* 54:2201–2218. <https://doi.org/10.1002/9783527610044.hetcat0065>
  45. Myers RH, Montgomery DC, Anderson-Cook CM (2016) *Response Surface Methodology: Process and Product Optimization Using Designed Experiments*. Wiley, New Jersey
  46. Ofomaja AE, Ho Y-S (2008) Effect of temperatures and pH on methyl violet biosorption by *Mansonia* wood sawdust. *Bioresour Technol* 99:5411–5417. <https://doi.org/10.1016/j.biortech.2007.11.018>
  47. Konkena B, Vasudevan S (2012) Understanding aqueous dispersibility of graphene oxide and reduced graphene oxide through pK<sub>a</sub> measurements. *J Phys Chem Lett* 3:867–872. <https://doi.org/10.1021/jz300236w>
  48. Su Q, Ye Q, Deng L, He Y, Cui X (2020) Prepared self-growth supported copper catalyst by recovering Cu(II) from wastewater using geopolymer microspheres. *J Clean Prod* 272:122571–122583. <https://doi.org/10.1016/j.jclepro.2020.122571>
  49. Şentürk İ, Alzein M (2020) Adsorptive removal of basic blue 41 using pistachio shell adsorbent - Performance in batch and column system. *Sustain Chem Pharm* 16:100254–100268. <https://doi.org/10.1016/j.scp.2020.100254>
  50. Wang H, Zhang P, Liu J (2017) Triethylene tetramine functionalized magnetic graphene oxide chitosan composite with superior capacity for the removal of phosphate. *J Chem Eng Data* 62:3341–3352. <https://doi.org/10.1021/acs.jced.7b00417>
  51. Jawad AH, Abdulhameed AS, Mastuli MS (2020) Mesoporous crosslinked chitosan-activated charcoal composite for the removal of thionine cationic dye: Comprehensive adsorption and mechanism study. *J Polym Environ* 28:1095–1105. <https://doi.org/10.1007/s10924-020-01671-5>
  52. Lagergren S (1898) About the theory of so-called adsorption of soluble substances. *K Sven Vetensk Akad Handl* 24:1–39
  53. Blanchard G, Maunaye M, Martin G (1984) Removal of heavy metals from waters by means of natural zeolites. *Water Res* 18:1501–1507. [https://doi.org/10.1016/0043-1354\(84\)90124-6](https://doi.org/10.1016/0043-1354(84)90124-6)
  54. Low MJD (1960) Kinetics of chemisorption of gases on solids. *Chem Rev* 60:267–312. <https://doi.org/10.1021/cr60205a003>

55. Marczewski AW (2010) Application of mixed order rate equations to adsorption of methylene blue on mesoporous carbons. *Appl Surf Sci* 256:5145–5152. <https://doi.org/10.1016/j.apsusc.2009.12.078>
56. Özer A (2007) Removal of Pb(II) ions from aqueous solutions by sulphuric acid-treated wheat bran. *J Hazard Mater* 141:753–761. <https://doi.org/10.1016/j.jhazmat.2006.07.040>
57. Azizian S, Fallah RN (2010) A new empirical rate equation for adsorption kinetics at solid/solution interface. *Appl Surf Sci* 256:5153–5156. <https://doi.org/10.1016/j.apsusc.2009.12.080>
58. Haerifar M, Azizian S (2012) Fractal-like adsorption kinetics at the solid/solution interface. *J Phys Chem C* 116:13111–13119. <https://doi.org/10.1021/jp301261h>
59. Haerifar M, Azizian S (2014) Fractal-like kinetics for adsorption on heterogeneous solid surfaces. *J Phys Chem C* 118:1129–1134. <https://doi.org/10.1021/jp4110882>
60. Balakrishnan N, Voinov V, Nikulin MS (2013) *Chi-Squared Goodness of Fit Tests with Applications*. Elsevier, Waltham
61. Bresnahan JL, Shapiro MM (1966) A general equation and technique for the exact partitioning of chi-square contingency tables. *Psychol Bull* 66:252–262. <https://doi.org/10.1037/h0023728>
62. Largitte L, Pasquier R (2016) A review of the kinetics adsorption models and their application to the adsorption of lead by an activated carbon. *Chem Eng Res Des* 109:495–504. <https://doi.org/10.1016/j.cherd.2016.02.006>
63. Nikzad S, Amooey AA, Alinejad-Mir A (2021) High effective removal of diazinon from aqueous solutions using the magnetic tragacanth-montmorillonite nanocomposite: isotherm, kinetic, and mechanism study. *Environ Sci Pollut Res* 28:20426–20439. <https://doi.org/10.1007/s11356-020-12238-1>
64. Xia F, Yang H, Li L, Ren Y, Shi D, Chai H, Ai H, He Q, Gu L (2020) Enhanced nitrate adsorption by using cetyltrimethylammonium chloride pre-loaded activated carbon. *Environ Technol* 41:3562–3572. <https://doi.org/10.1080/09593330.2019.1615133>
65. Ofomaja AE (2010) Intraparticle diffusion process for lead(II) biosorption onto mansonia wood sawdust. *Bioresour Technol* 101:5868–5876. <https://doi.org/10.1016/j.biortech.2010.03.033>
66. Omidi S, Kakanejadifard A (2018) Eco-friendly synthesis of graphene-chitosan composite hydrogel as efficient adsorbent for Congo red. *RSC Adv* 8:12179–12189. <https://doi.org/10.1039/c8ra00510a>
67. Langmuir I (1918) The adsorption of gases on plane surfaces of glass, mica and platinum. *J Am Chem Soc* 40:1361–1403. <https://doi.org/10.1021/ja02242a004>
68. Freundlich HMF (1906) Over the adsorption in solution. *J Phys Chem* 57:385–471
69. Temkin M, Pyzhev V (1940) Kinetics of ammonia synthesis on promoted iron catalysts. *Acta Physicochim URSS* 12:327–356
70. Azizian S, Eris S, Wilson LD (2018) Re-evaluation of the century-old Langmuir isotherm for modeling adsorption phenomena in solution. *Chem Phys* 513:99–104. <https://doi.org/10.1016/j.chemphys.2018.06.022>
71. Redlich O, Peterson DL (1959) A useful adsorption isotherm. *J Phys Chem* 63:1024–1030. <https://doi.org/10.1021/j150576a611>
72. Toth J (1971) State equation of the solid-gas interface layers. *Acta Chim Acad Sci Hung* 69:311–328
73. Yao C (2000) Extended and improved Langmuir equation for correlating adsorption equilibrium data. *Sep Purif Technol* 19:237–242. [https://doi.org/10.1016/S1383-5866\(00\)00060-5](https://doi.org/10.1016/S1383-5866(00)00060-5)
74. Sips R (1948) On the structure of a catalyst surface. *J Chem Phys* 16:490–495. <https://doi.org/10.1063/1.1746922>
75. Saravanan P, Josephraj J, Thillainayagam BP, Ravindiran G (2021) Evaluation of the adsorptive removal of cationic dyes by greening biochar derived from agricultural bio-waste of rice husk. *Biomass Convers Biorefin*. <https://doi.org/10.1007/s13399-021-01415-y>
76. El-Gendy NS, El-Salamony RA, Amr SSA, Nassar HN (2015) Statistical optimization of Basic Blue 41 dye biosorption by *saccharomyces cerevisiae* spent waste biomass and photo-catalytic regeneration using acid TiO<sub>2</sub> hydrosol. *J Water Process Eng* 6:193–202. <https://doi.org/10.1016/j.jwpe.2015.04.007>
77. Nouri L, Hemidouche S, Boudjema A, Kaouah F, Sadaoui Z, Bachari K (2020) Elaboration and characterization of photobiocomposite beads, based on titanium (IV) oxide and sodium alginate biopolymer, for basic blue 41 adsorption/photocatalytic degradation. *Int J Biol Macromol* 151:66–84. <https://doi.org/10.1016/j.ijbiomac.2020.02.159>
78. Humelnicu I, Băiceanu A, Ignat ME, Dulman V (2017) The removal of basic blue 41 textile dye from aqueous solution by adsorption onto natural zeolitic tuff: Kinetics and thermodynamics. *Process Saf Environ Prot* 105:274–287. <https://doi.org/10.1016/j.psep.2016.11.016>

# Figures

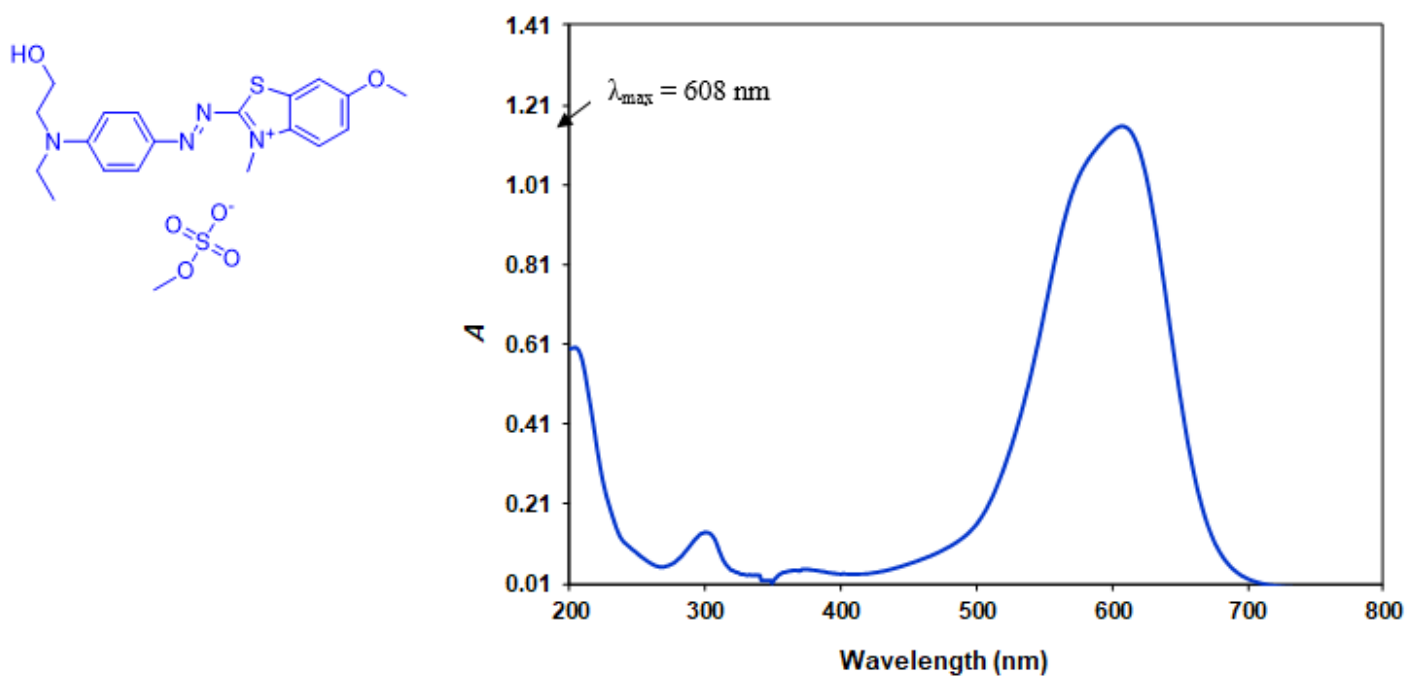


Figure 1

Structure and UV-Vis absorption spectrum of basic blue 41 at concentration of  $10.0 \text{ mg}\cdot\text{L}^{-1}$  and pH of 6.5

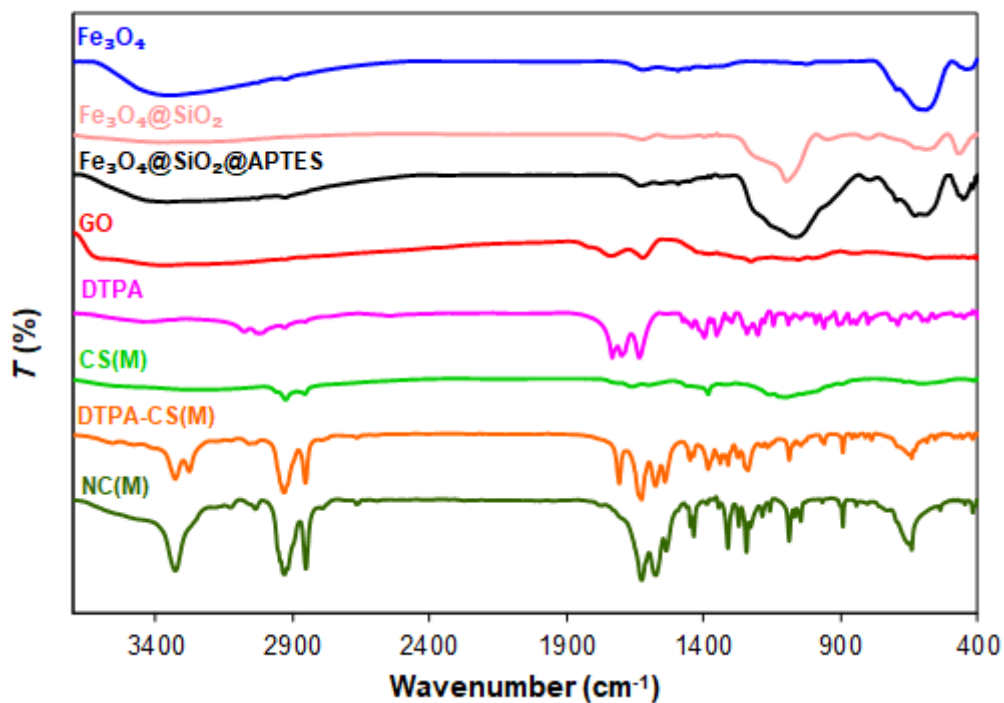


Figure 2

FT-IR spectra of Fe<sub>3</sub>O<sub>4</sub>, Fe<sub>3</sub>O<sub>4</sub>@SiO<sub>2</sub>, Fe<sub>3</sub>O<sub>4</sub>@SiO<sub>2</sub>@APTES, GO, DTPA-CS(M), and NC(M)

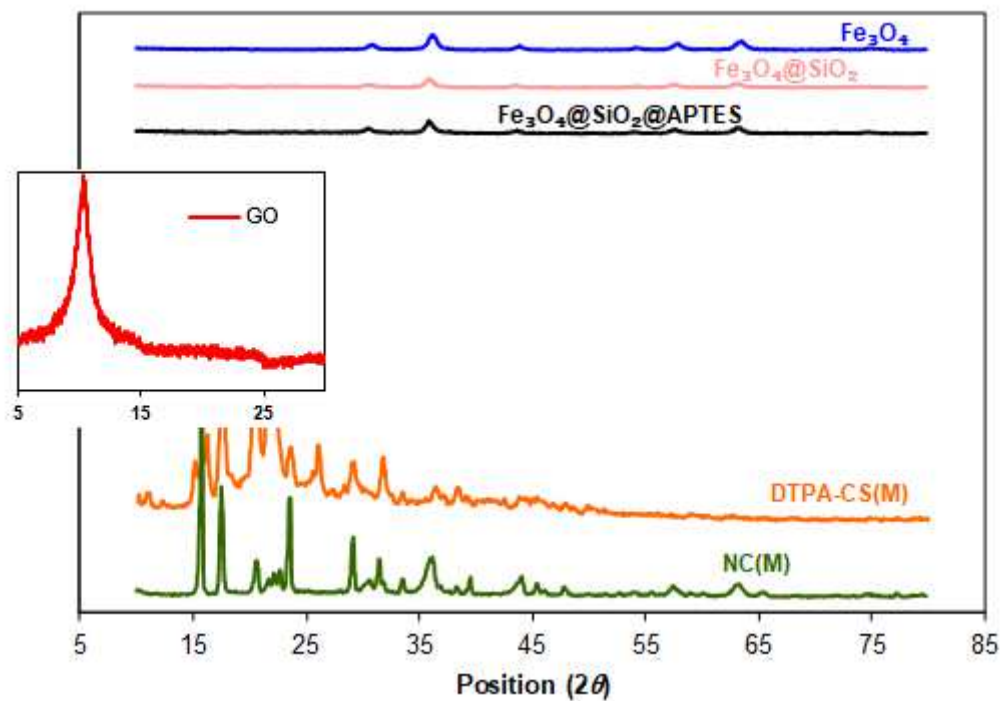


Figure 3

XRD patterns of Fe<sub>3</sub>O<sub>4</sub>, Fe<sub>3</sub>O<sub>4</sub>@SiO<sub>2</sub>, Fe<sub>3</sub>O<sub>4</sub>@SiO<sub>2</sub>@APTES, GO, DTPA-CS(M), and NC(M)

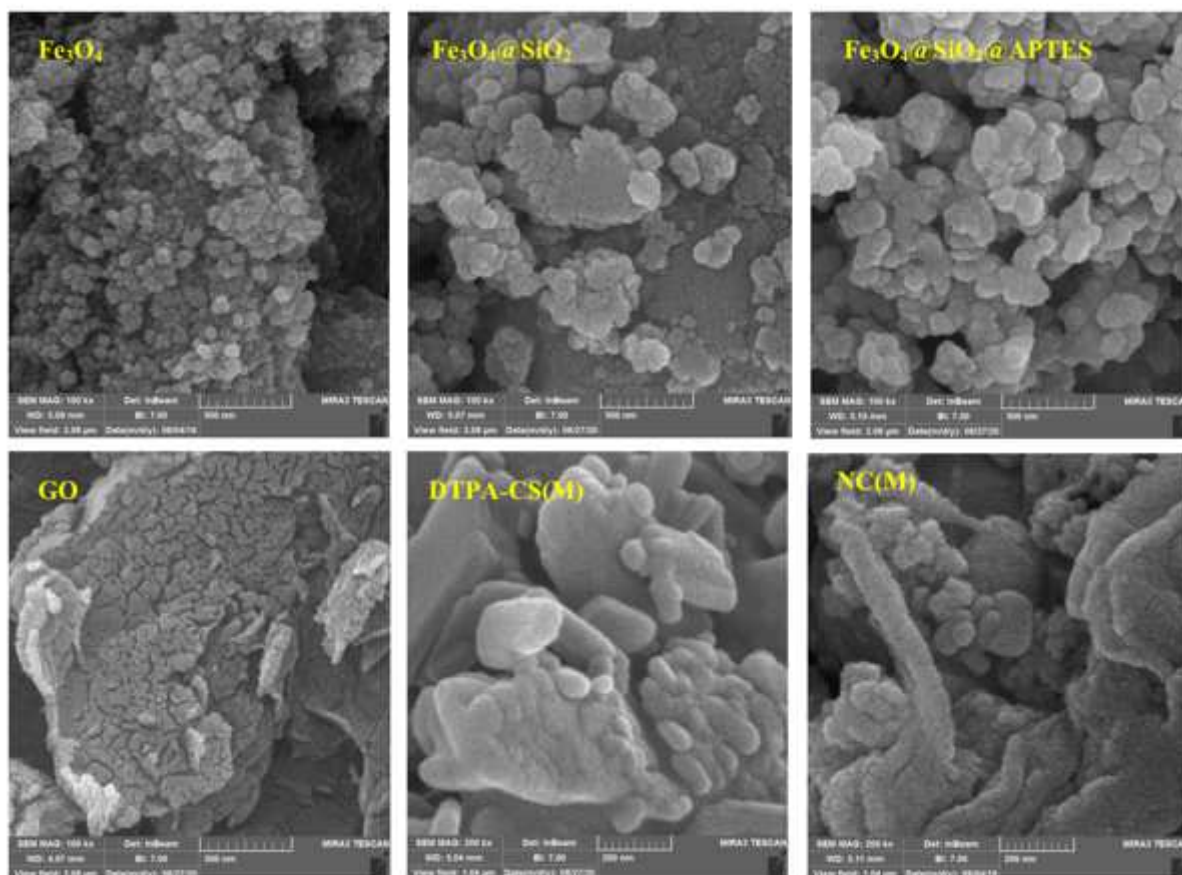


Figure 4

FESEM images of Fe<sub>3</sub>O<sub>4</sub>, Fe<sub>3</sub>O<sub>4</sub>@SiO<sub>2</sub>, Fe<sub>3</sub>O<sub>4</sub>@SiO<sub>2</sub>@APTES, GO, DTPA-CS(M), and NC(M)

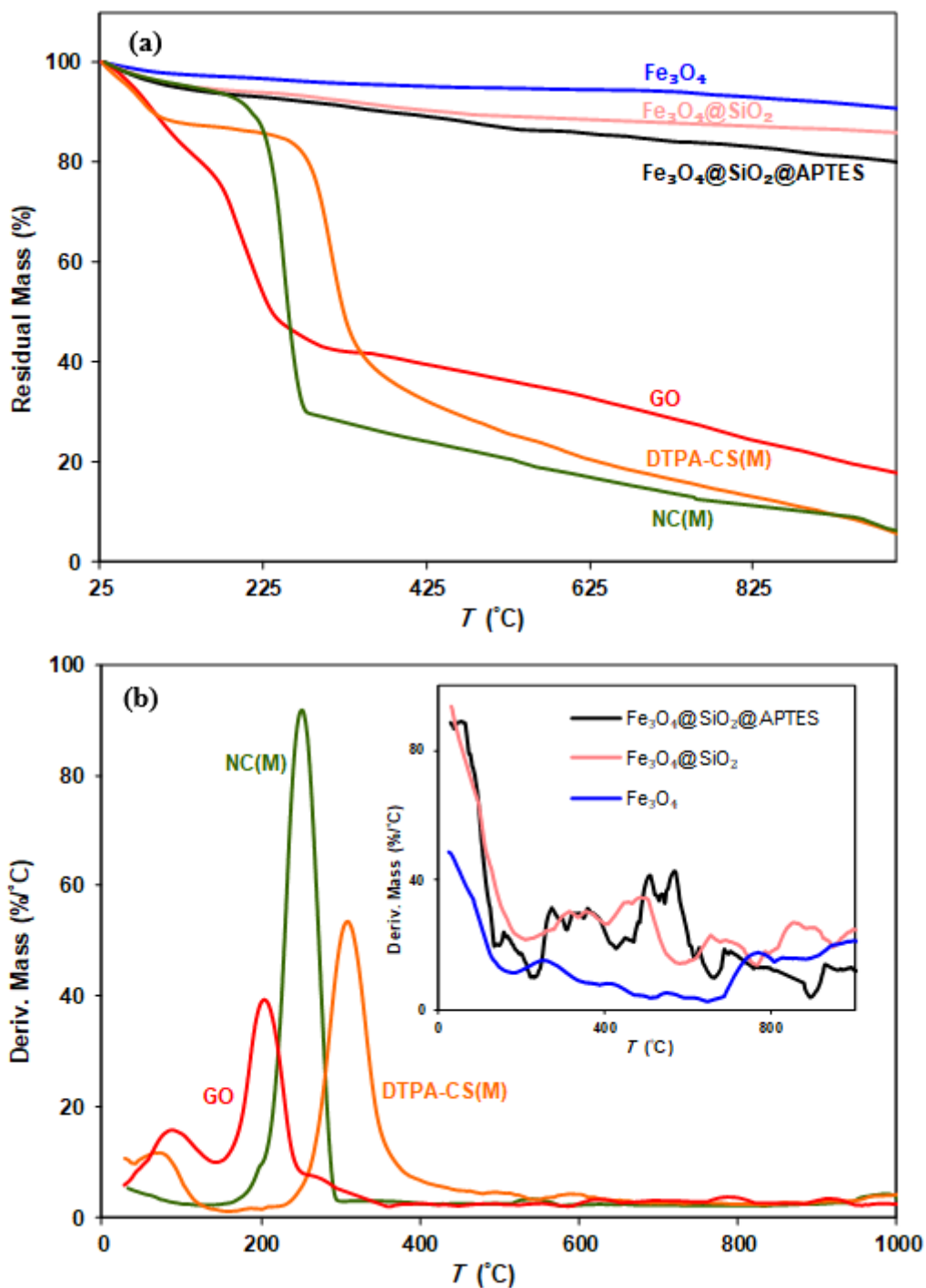


Figure 5

(a) TGA and (b) DTG curves of Fe<sub>3</sub>O<sub>4</sub>, Fe<sub>3</sub>O<sub>4</sub>@SiO<sub>2</sub>, Fe<sub>3</sub>O<sub>4</sub>@SiO<sub>2</sub>@APTES, GO, DTPA-CS(M), and NC(M)

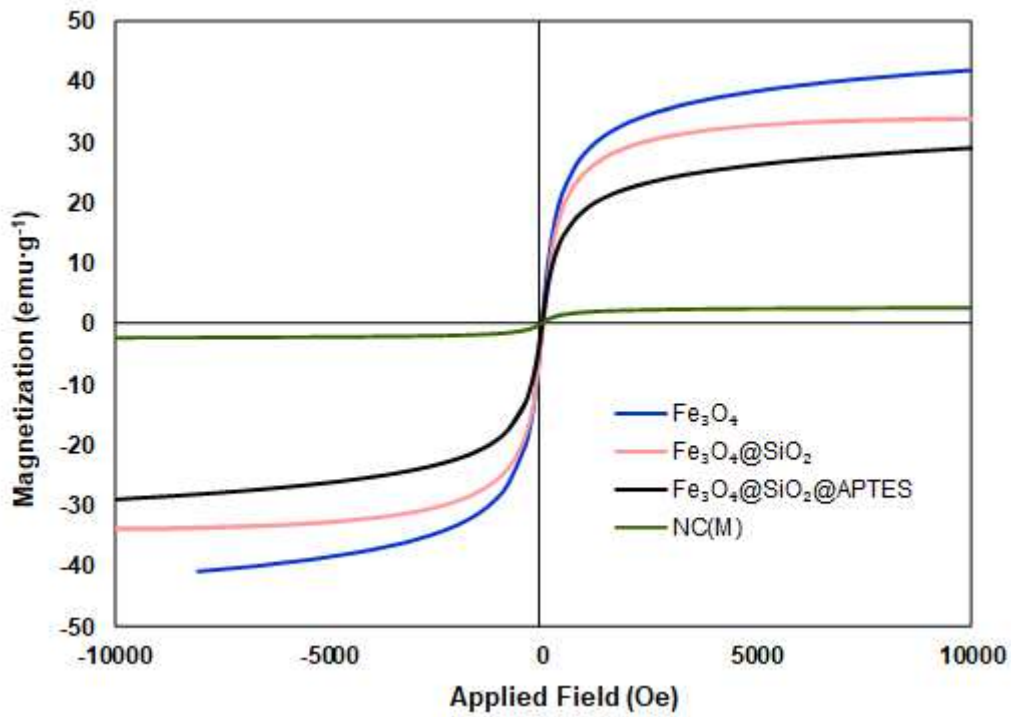


Figure 6

Magnetization measurements for Fe<sub>3</sub>O<sub>4</sub>, Fe<sub>3</sub>O<sub>4</sub>@SiO<sub>2</sub>, Fe<sub>3</sub>O<sub>4</sub>@SiO<sub>2</sub>@APTES and NC(M)

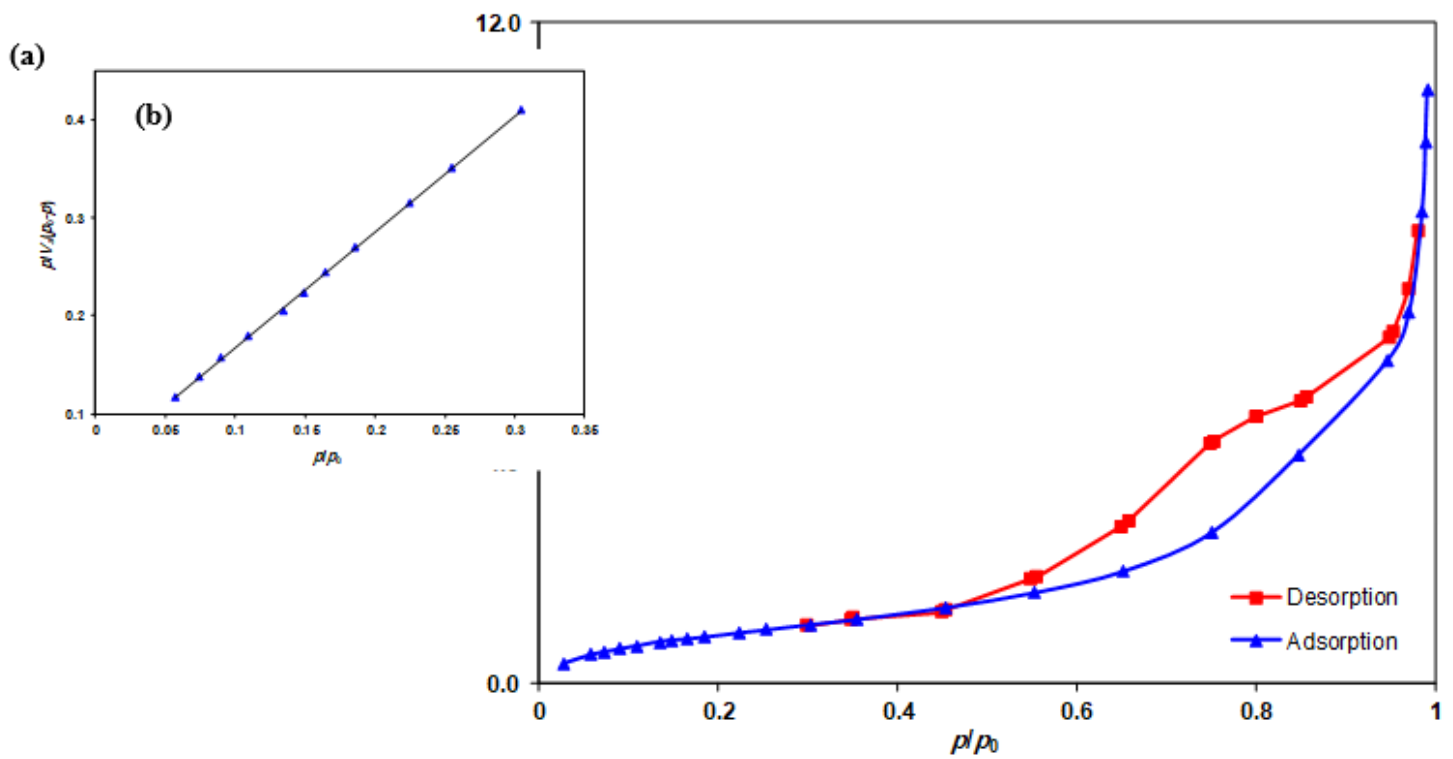


Figure 7

(a) N<sub>2</sub> adsorption/desorption isotherm at 77 K, (b) BET plot of NC(M)

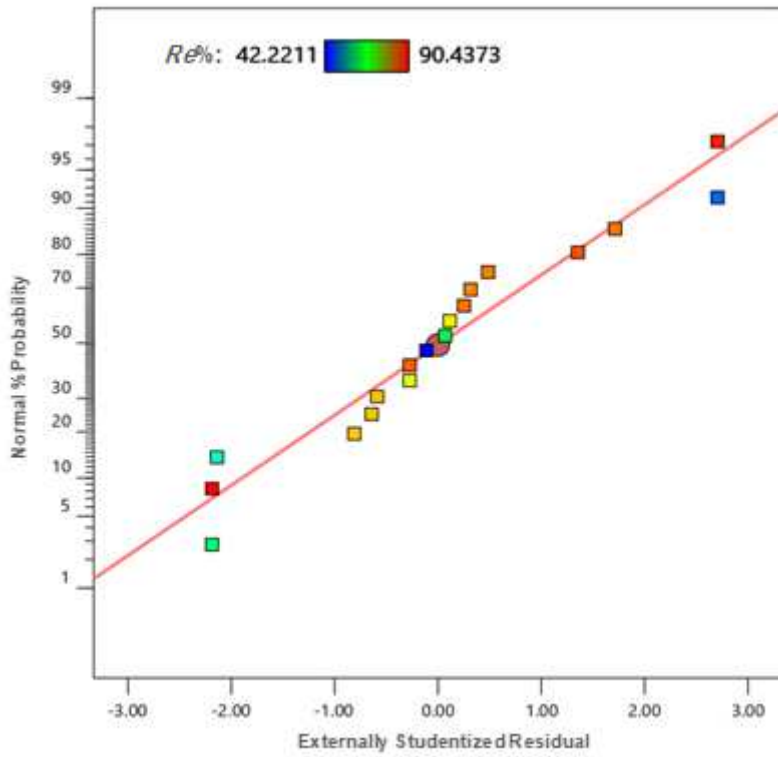


Figure 8

Normal plot of residuals

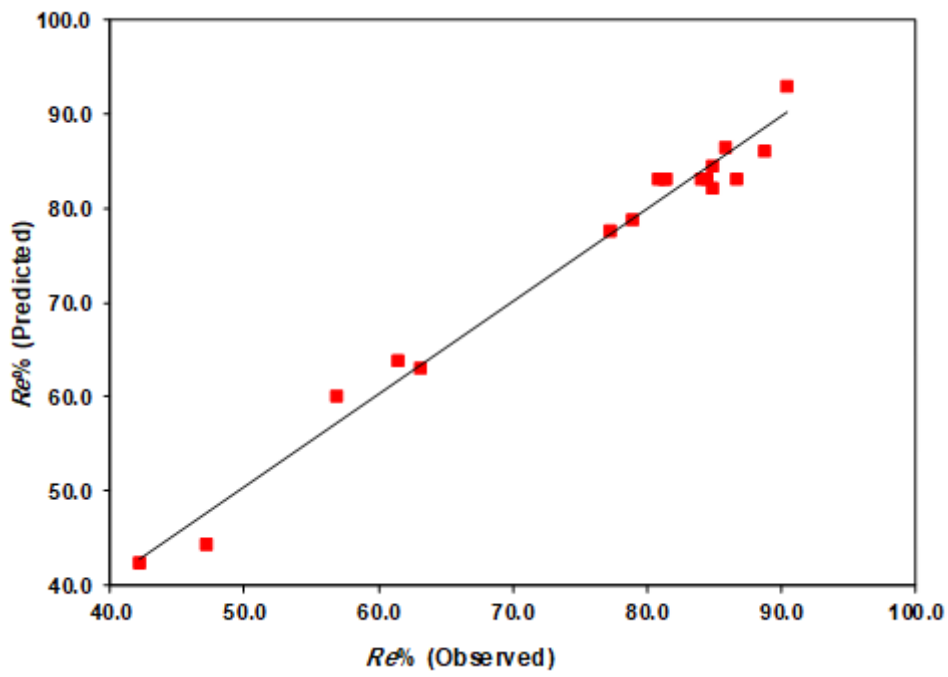


Figure 9

Plot of predicted response versus observed response

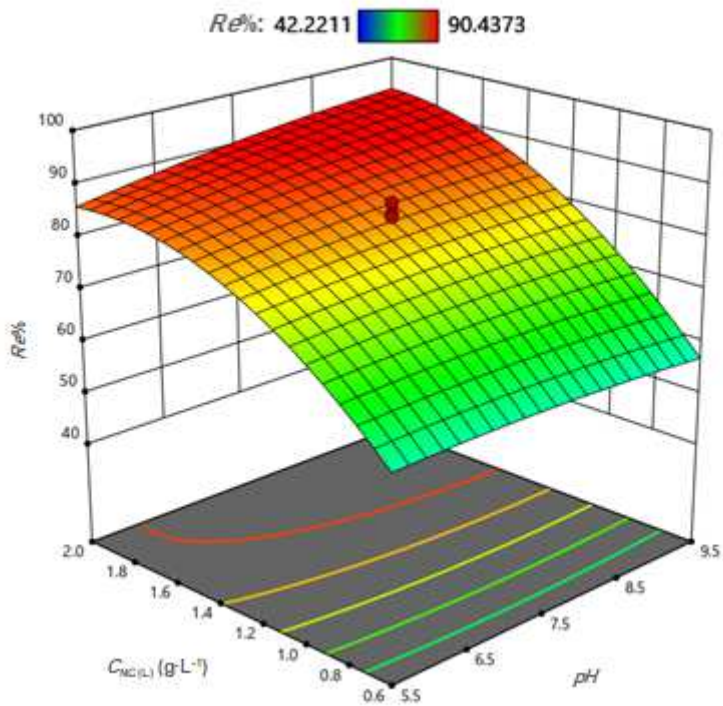


Figure 10

Response surface plot for percentage of dye removal as a function of nanocomposite concentration and initial pH at temperature of 43.0 °C

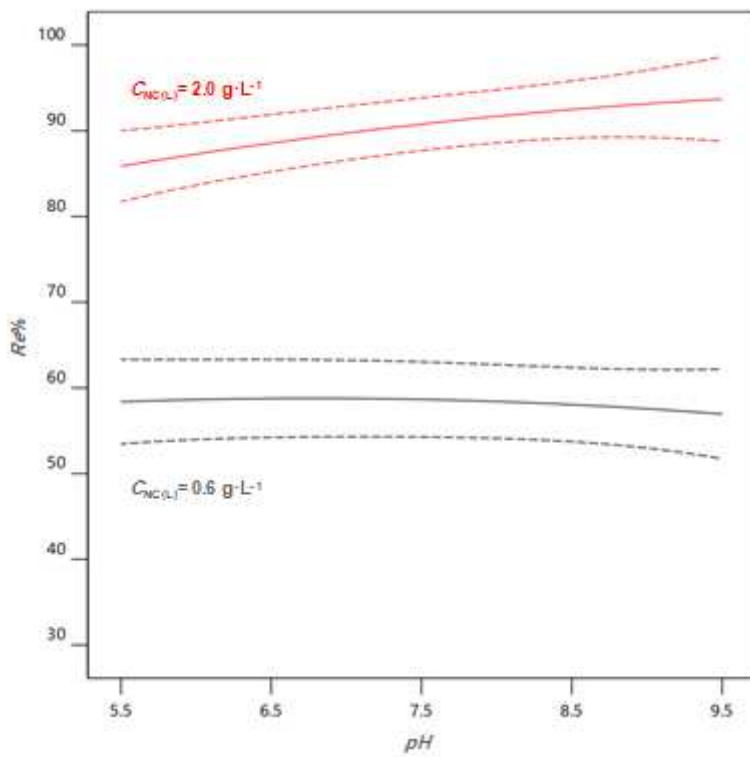


Figure 11

Percentage of dye removal versus pH at two different nanocomposite concentrations with 95% confidence interval and temperature of 43.0 °C

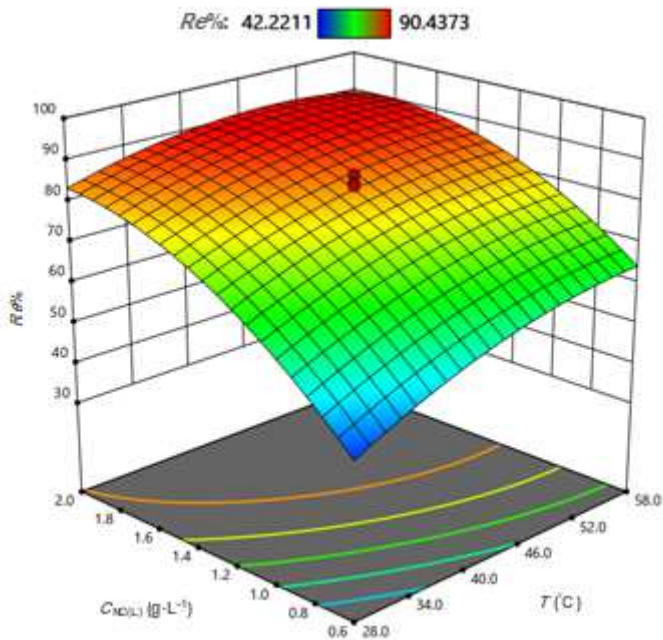


Figure 12

Response surface plot for percentage of dye removal as a function of nanocomposite concentration and temperature at pH of 7.50

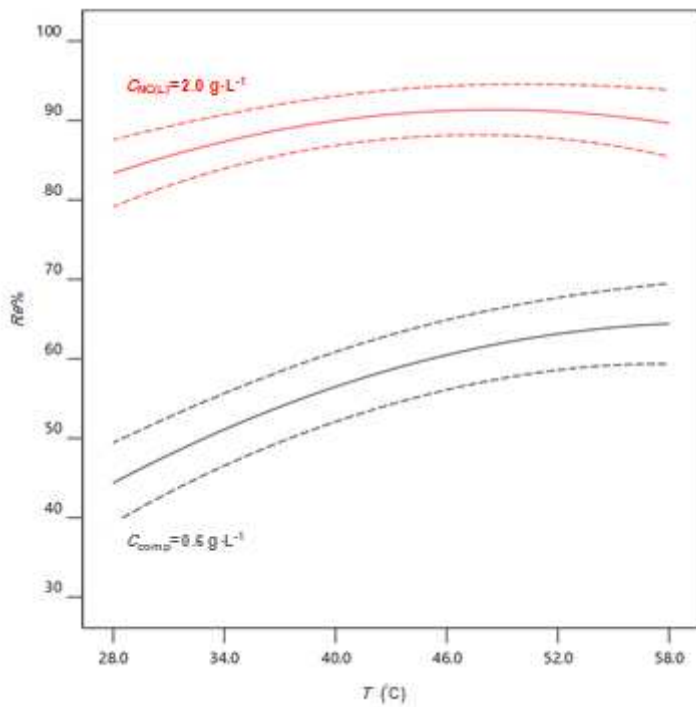


Figure 13

Percentage of dye removal versus temperature at two different nanocomposite concentrations with 95% confidence interval and pH of 7.50

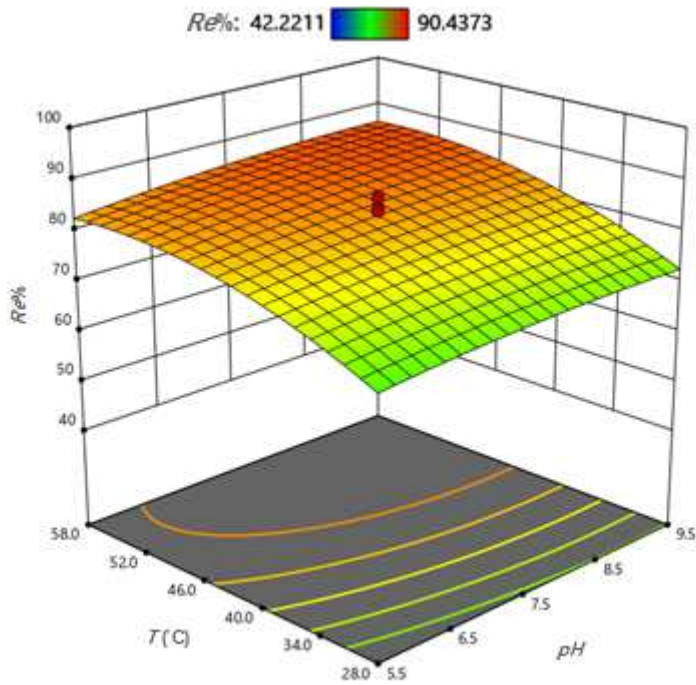


Figure 14

Response surface plot for percentage of dye removal as a function of pH and temperature at nanocomposite concentration of 1.30 g·L<sup>-1</sup>

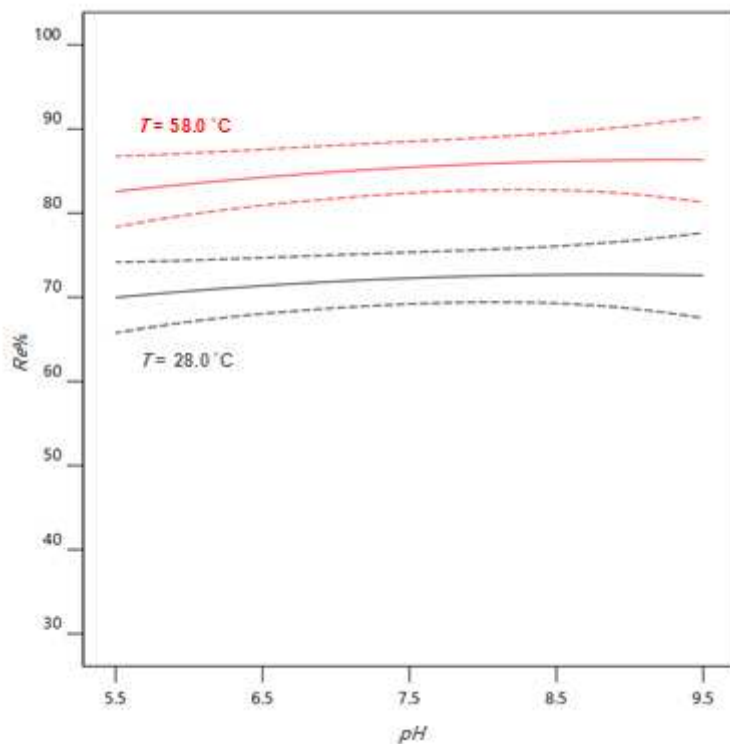


Figure 15

Percentage of dye removal versus pH at two temperatures with 95% confidence interval and nanocomposite concentration of 1.30 g·L<sup>-1</sup>

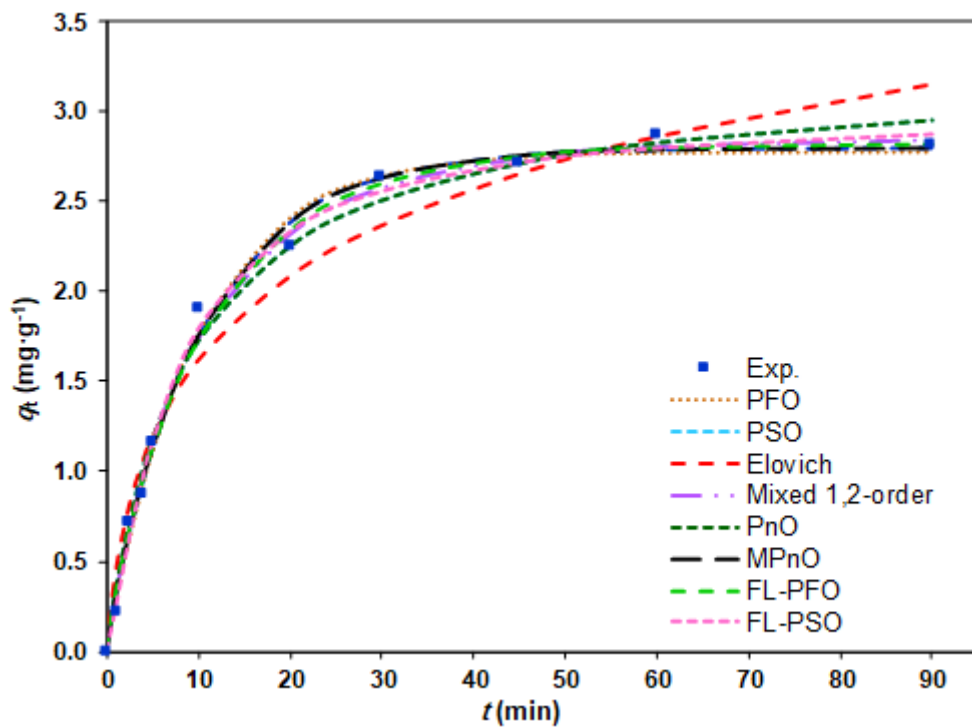
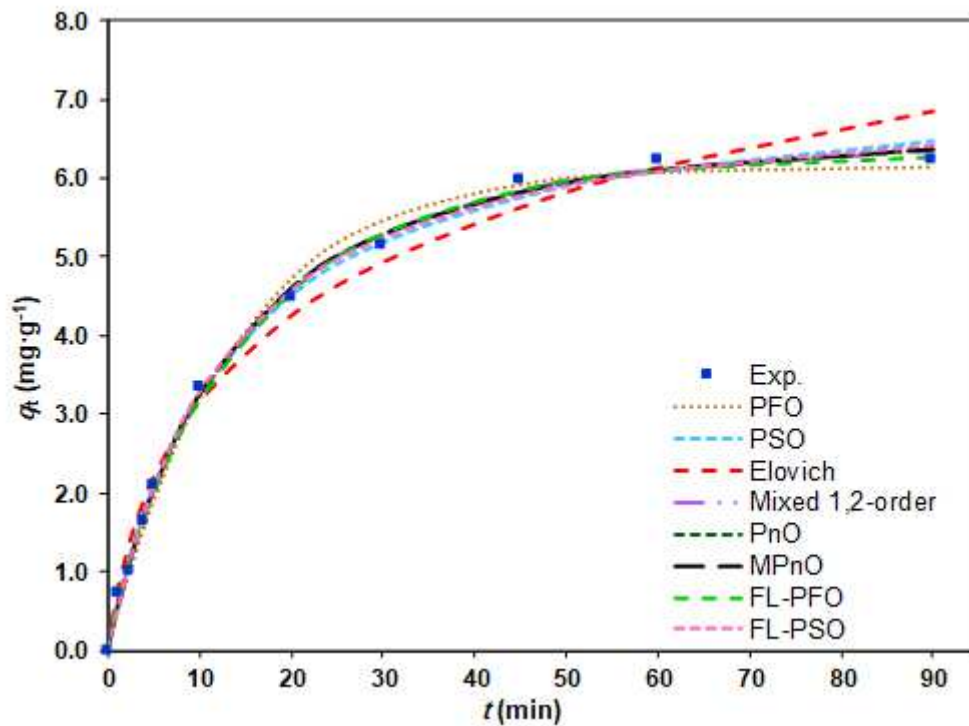


Figure 16

Experimental and fitted kinetics data for adsorption of BB41 with concentration of 8.0 mg·L<sup>-1</sup> under optimum conditions



**Figure 17**

Experimental and fitted kinetics data for adsorption of BB41 with concentration of 15.0 mg·L<sup>-1</sup> under optimum conditions

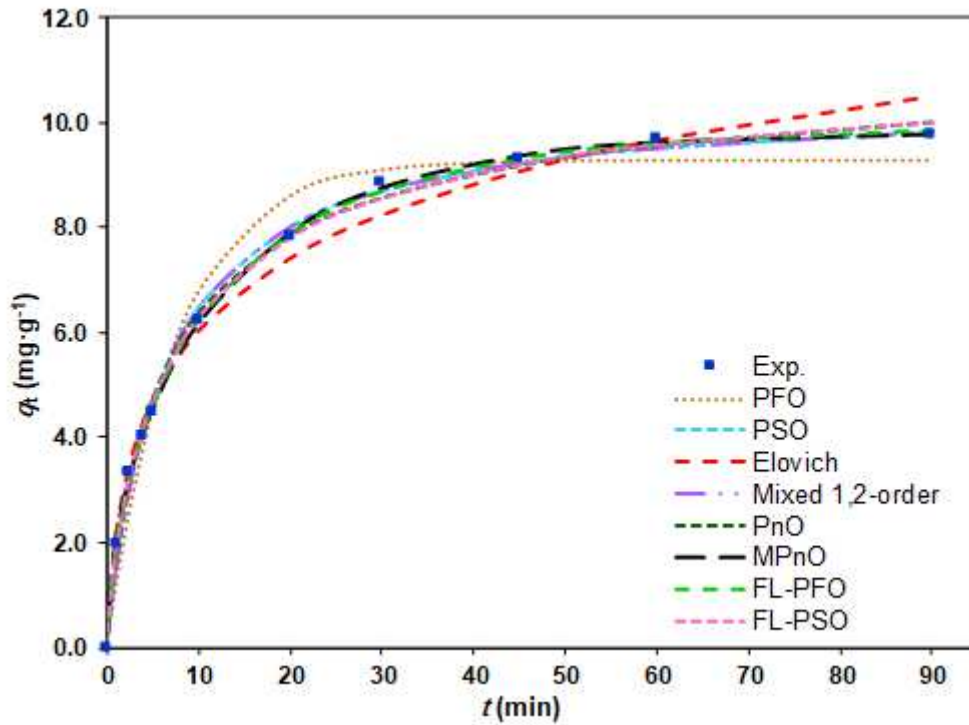


**Figure 18**

Experimental and fitted kinetics data for adsorption of BB41 with concentration of 30.0 mg·L<sup>-1</sup> under optimum conditions

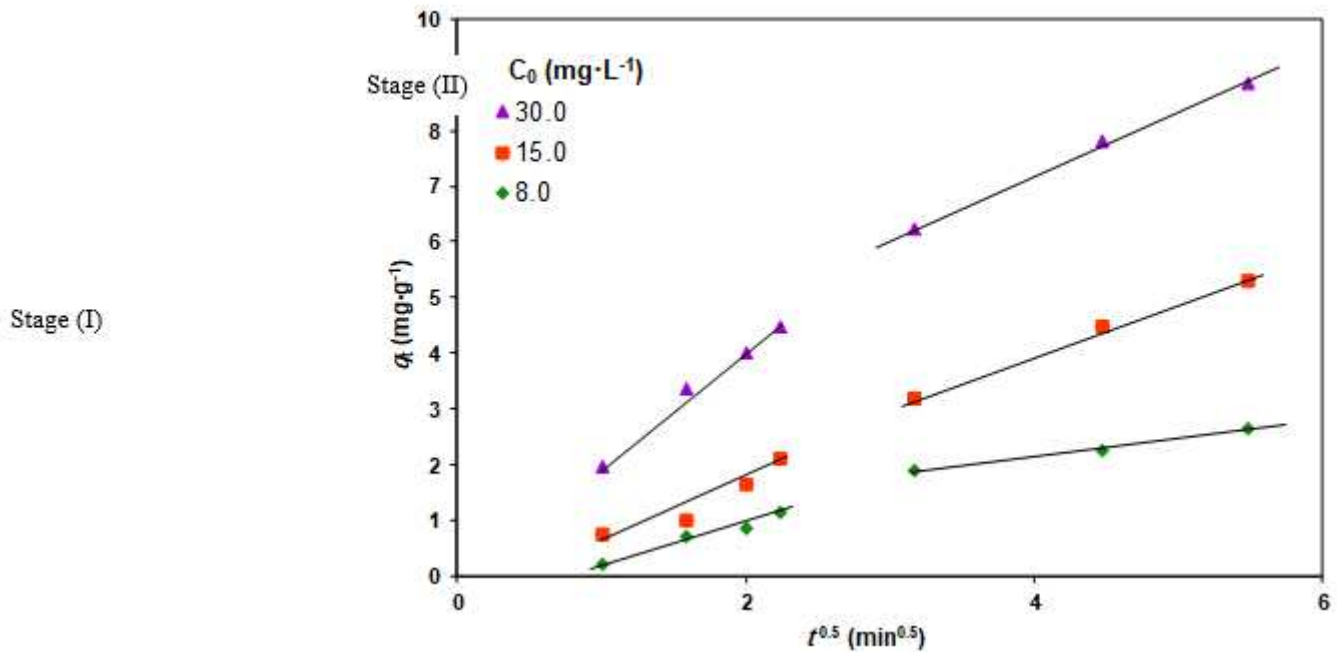


Figure 19

Intra-particle diffusion plot for BB41 adsorption at different concentrations under optimum conditions

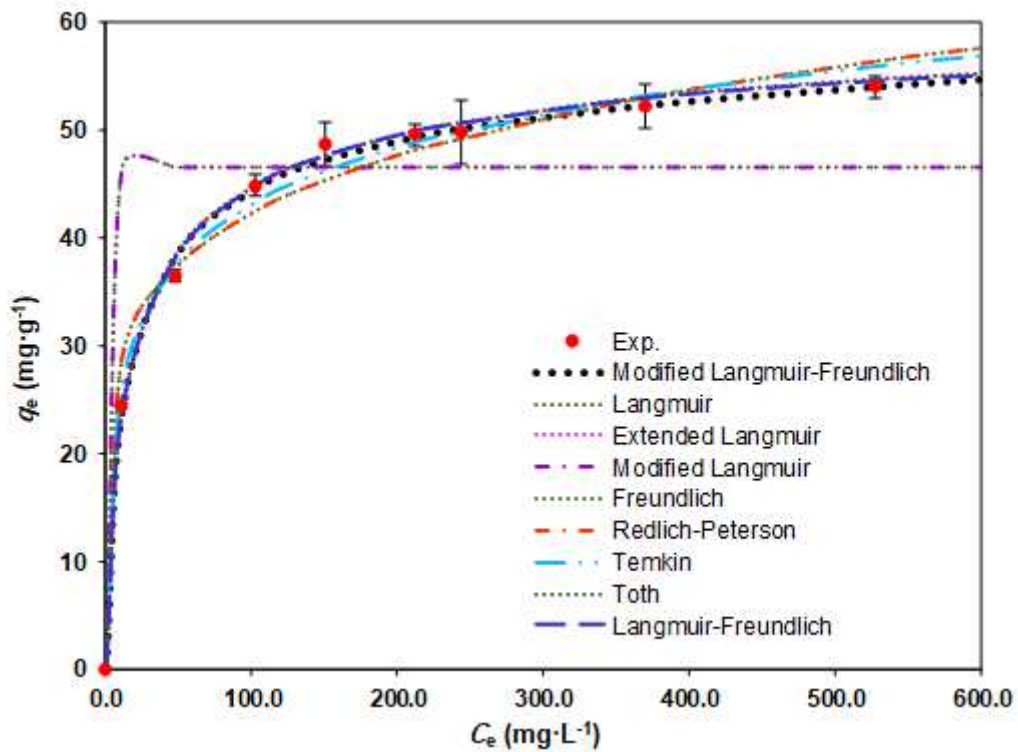


Figure 20

Adsorption isotherms for adsorption of BB41 under optimum conditions

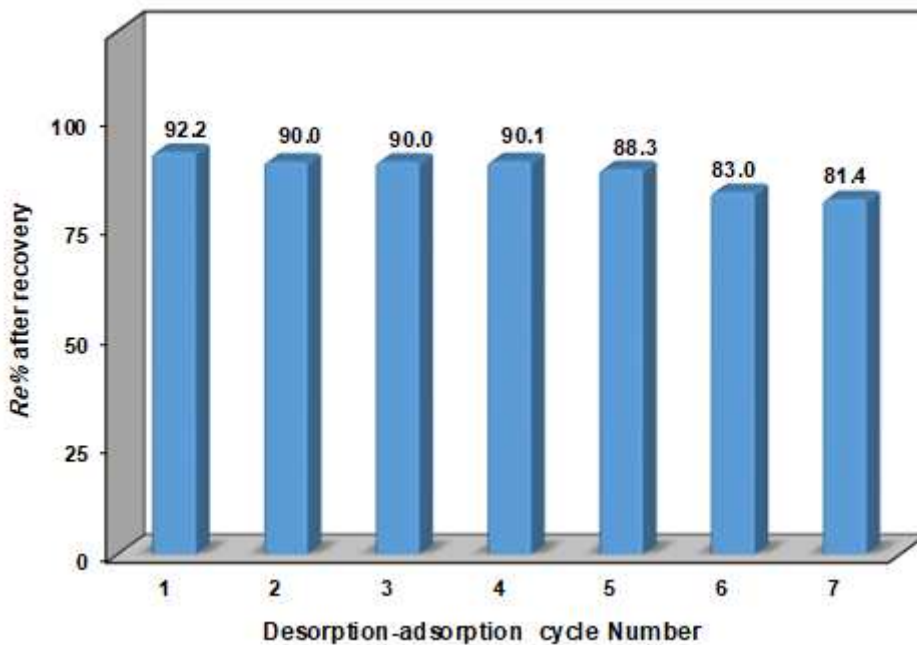


Figure 21

Percentage of dye removal after recovery

## Supplementary Files

This is a list of supplementary files associated with this preprint. Click to download.

- [SupplementaryInformation.docx](#)
- [GraphicalAbstract.png](#)